Pontifícia Universidade Católica
do Rio de Janeiro

Rafael Muffato Reis

Towards quantum control of levitated mesoscopic particles

Tese de Doutorado

Thesis presented to the Programa de Pós–graduação em Física of PUC-Rio in partial fulfillment of the requirements for the degree of Doutor em Ciências - Física.

Advisor: Prof. Thiago Barbosa dos Santos Guerreiro

Rio de Janeiro
February 2025

Pontifícia Universidade Católica
do Rio de Janeiro

Rafael Muffato Reis

Towards quantum control of levitated mesoscopic particles

Thesis presented to the Programa de Pós–graduação em Física of PUC-Rio in partial fulfillment of the requirements for the degree of Doutor em Ciências - Física. Approved by the Examination Committee:

Prof. Thiago Barbosa dos Santos Guerreiro
Advisor
Departamento de Física – PUC-Rio

Prof. Antonio Zelaquett Khoury
UFF

Prof. Paulo Américo Maia Neto
UFRJ

Prof. Thiago Pedro Mayer Alegre
UNICAMP

Prof. Hendrik Ulbrichit
University of Southampton

Rio de Janeiro, February 4th, 2025

Rafael Muffato Reis

Graduated in physics by the Universidade Estadual de Maringá.

Bibliographic data

Reis, Rafael Muffato

Towards quantum control of levitated mesoscopic particles / Rafael Muffato Reis; advisor: Thiago Barbosa dos Santos Guerreiro. – 2025.

90 f: il. color. ; 30 cm

Tese (doutorado) - Pontifícia Universidade Católica do Rio de Janeiro, Departamento de Física, 2025.

Inclui bibliografia

1. Física – Teses. 2. Optomecânica. 3. Pinça óptica. 4. Sistemas quânticos mesoscópicos. I. Guerreiro, Thiago. II. Pontifícia Universidade Católica do Rio de Janeiro. Departamento de Física. III. Título.

CDD: 004

To my parents, for their support
and encouragement.

Acknowledgments

To my adviser Professor Thiago Guerreiro for the stimulus and partnership to carry out this work.

To Hendrik Ulbricht for hosting me in his research group under LeviNet Scientific Missions scheme.

I would like to express my deep gratitude to my friends and colleagues for their unwavering support, encouragement, and camaraderie throughout this journey. Your insights, feedback, and shared moments of laughter have been invaluable in making this process not only achievable but also meaningful. Thank you for being an integral part of this chapter in my life.

To CNPq and PUC-Rio, for the aids granted, without which this work could not have been accomplished.

This study was financed in part by the Coordenação de Aperfeiçoamento de Pessoal de Nível Superior - Brasil (CAPES) - Finance Code 001.

Abstract

Reis, Rafael Muffato; Guerreiro, Thiago (Advisor). **Towards quantum control of levitated mesoscopic particles**. Rio de Janeiro, 2025. 90p. Tese de Doutorado – Departamento de Física, Pontifícia Universidade Católica do Rio de Janeiro.

Levitated optomechanics experiments are steadily approaching the quantum regime. In this thesis, we explore the extrinsic coupling of levitated nanoparticles in optical tweezers in vacuum, with nonlinearities induced by optical and electrical control. Furthermore, we present a technique for the preparation of non-Gaussian states of the center-of-mass motion of these particles, leveraging both parametric modulation and the intrinsic nonlinearity of the optical potential. Additionally, a quantum model for optical detection with structured light fields is developed, enabling the analysis of a proposed experiment designed to minimize and control perturbations due to position measurement. These advances pave the way for refined control and manipulation of quantum states in levitated systems in the near future.

Keywords

Optomechanics; Optical tweezer; Mesoscopic quantum systems.

Resumo

Reis, Rafael Muffato; Guerreiro, Thiago. **Rumo ao controle quântico de partículas mesoscópicas levitadas**. Rio de Janeiro, 2025. 90p. Tese de Doutorado – Departamento de Física, Pontifícia Universidade Católica do Rio de Janeiro.

Experimentos de optomecânica levitada se aproximam cada vez mais do regime quântico. Nesta tese, exploramos o acoplamento extrínseco de nanopartículas levitadas em pinças ópticas em vácuo com não-linearidades induzidas por controle óptico e elétrico. Além disso, apresentamos uma técnica para preparação de estados não-Gaussianos do movimento do centro de massa de tais partículas, utilizando tanto modulação paramétrica quanto a não-linearidade intrínseca do potencial óptico. Adicionalmente, um modelo quântico para detecção óptica com campos de luz estruturados é desenvolvido, permitindo a análise de uma proposta de experimento projetada para minimizar e controlar perturbações devido à medida de posição. Tais avanços abrem caminho para o controle refinado e manipulação de estados quânticos em sistemas levitados no futuro próximo.

Palavras-chave

Optomecânica; Pinça óptica; Sistemas quânticos mesoscópicos.

Table of contents

List of figures

List of tables

List of Abreviations

COM – Centre of Mass

PSD – Power Spectral Density

EOM – Eletro Optical Modulator

What we observe is not nature itself, but nature exposed to our method of questioning.

Werner Heisenberg, *Physics and Philosophy: The Revolution in Modern Science.*

1
Introduction

1.1
Levitodynamics

Light interacts with matter. In 1619, Kepler proposed that light could affect a comet's tails explaining why it consistently point away from the Sun [1]. This concept was eventually formalized with Maxwell's theory of electromagnetism, where the transfer of momentum by light was quantified [2]. Preliminary experiments regarding this phenomenon were first verified at the turn of the 20th century [3, 4], around the same time when Einstein discussed the momentum transfer of light [5].

In the sixties Braginsky analysed theoretically and showed experimentally that microwaves can affect the mechanical energy of an oscillating mirror [6, 7]. His work is foundational for modern concepts in quantum measurement, as well as developing technologies like gravitational wave detectors where such effects play a critical role. However, these optical forces are so small that only after the invention of the LASER that Arthur Ashkin was able truly control the movement of small particles. He observed that a laser beam can push these particles in the direction of its propagation due to the radiation pressure exerted by the light. This force is known as the scattering force, F_{scatt}. More intriguingly, he also observed that particles with refractive indices higher than that of the surrounding medium were drawn toward the center of the laser's focal point. The force responsible for this attraction is known as the gradient force, F_{grad}. The gradient force enabled the development of single-beam optical tweezers, allowing for the precise manipulation of microscopic particles [8]. The discussion on quantum aspects of noise in interferometers were further developed by [9] setting up the field of quantum optomechanics in the 1990s [10, 11].

In typical optical levitation experiments, a dielectric nanoparticle is trapped using a tightly focused Gaussian beam, which generates a confining potential that is approximately harmonic [12, 13, 14]. By controlling the trapping laser power it becomes possible to precisely control the conservative dynamics and change the oscillator's natural frequency, Ω_0, within an approximate range of $50 \sim 500$ kHz. Moreover, the ability to levitate particles without mechanical clamping in ultra-high vacuum conditions allows for exceptional decoupling from the environment with extremely low damping Γ_0. As a result, the energy

lost in an oscillator per oscillation relative to the stored mechanical energy is very small with quality factor, $Q = \Omega_0/\Gamma_0$, reaching remarkable values of up to 10^{10} [15]. Optically levitated nanoparticles [16] offer a promising experimental platform for studying non-equilibrium physics, detecting small forces, advancing material science, and testing the principles of quantum mechanics.

1.2 Matterwave interferometry

Quantum mechanics describes the behavior of particles at very small scales, such as atoms and subatomic particles, where the rules of classical physics no longer apply. One of the core concepts in quantum mechanics is superposition.

In classical physics, objects exist in well-defined states—like a car being in one location or a switch being either "on" or "off." However, in the quantum realm, particles can exist in a superposition of multiple states simultaneously. For example, an electron can be in two places at once or occupy multiple energy levels at the same time. The particle remains in this superposed state until it is measured or observed, at which point the superposition collapses, and the particle takes on a single, definite state.

Superposition is fundamental to many emerging quantum technologies. In quantum computing, it enables faster processing of complex problems in cryptography, drug discovery, and materials science. Quantum sensing leverages superposition for unprecedented precision in measuring time, magnetic fields, and gravitational forces, enhancing technologies like GPS and medical imaging. In quantum communication, superposition allows for highly secure data transmission, with quantum cryptography ensuring eavesdropping is detectable. Finally, quantum simulations utilize superposition to model complex systems, leading to breakthroughs in understanding new materials and particle behavior.

The extension of quantum phenomena, typically seen at microscopic scales, to manifest in larger systems is refereed as macroscopic quantum states. These states are not readily observed and become increasingly difficult to produce as the mass and size of the system increases [17]. There is significant interest in researching these states, as they are crucial for advancing quantum technologies, particularly highly sensitive quantum sensors, and for addressing fundamental questions in physics. They play a key role in testing the limits of quantum mechanics and exploring the influence of gravity on quantum systems [18].

The concept of superposition, first demonstrated in Young's double-

Figure 1.1: five steps for interferometry

slit experiment with light [19], was later extended to particles through the discovery of electron wave-particle duality [20]. Experiments on matter-wave interferometry has since shown that larger particles, such as fullerenes with masses around 60 atomic mass units (amu), can also exist in superposition states [21]. As experimental techniques have advanced, the mass of particles exhibiting quantum interference has steadily increased, reaching over 10,000 amu [22] and beyond 25 kDa [23]. This bottom-up progression raises the intriguing question of how massive a superposition state can be prepared.

Experiments with the centre of mass (COM) motion of levitated nanoparticles offers an outstanding level of decoupling from the environment, as such they are considered as a promising platform for testing quantum mechanics at larger scales. A milestone in reaching the quantum regime of levitated nanoparticle's COM motion has been achieved through ground-state cooling by several groups [24, 25, 26, 27, 28]. Transforming these cooled states into superposition is yet to be achieved. Recent research with levitated optomechanical setups is aiming to do that [29, 30, 31] with efforts on improving experimental setups [32, 33]. These ongoing efforts aims to extend matter-wave interferometry in a top down approach to nanoparticles with masses up to 10^9 amu. In this thesis I will also discuss an approach to do that.

1.3 Procedure for interferometry

A quantum interference experiment is a reliable method for demonstrating the preparation of quantum superposition states. There are five key processes are essential and worth mentioning for such an experiment.

1. The first step is the previously mentioned ground-state cooling. These cooled states act as the initial coherent source upon which the quantum superposition will be generated.

2. Secondly, coherent wave-function expansion must happen to delocalize the particle's state [33, 34] over distances larger than its radius. This is necessary because, although the ground state has an uncertainty on the order of picometers, the physical size of the nanosphere is on the order of nanometers. This significant difference causes the particle nature of the

nanosphere to manifest itself. When the wave function extends beyond the object's physical size, wave-like properties increasingly dominate its behavior, making quantum superpositions possible to occur.

3. After expansion, a nonlinear operation is needed to induce quantum superposition to the state. This nonlinear operation is represented by the slits in the double-slit experiment. This is a crucial step that transforms the state inducing phenomena that can not be described by classical physics alone. Although cooled and latter expanded states, may hint at quantum behavior through squeezing, for example, they are still Gaussian states and considered insufficient by some to provide conclusive evidence of quantum behavior [35]. Thus, a nonlinear operation is required to generate interference patterns and unequivocally confirm the quantum nature of the system in a qualitatively new way beyond the scope of classical physics.

   A few sources of non linearity have been discussed. Some of them use laser light in a standing wave configuration [36]. Some other suggest using electrical trapping [37]. The work discussed in this thesis uses the intrinsic non linear tails of optical potential generated by a single focused Gaussian laser beam.

4. The definitive hallmark of quantum behavior is the observation of interference fringes, which unambiguously demonstrate quantum superposition. The experimental procedure requires a way to verify these interference fringes or reconstruct the quantum Wigner function, including its negativity. Optomechanical state tomography has been successfully demonstrated in the classical regime for clamped [38] and levitated [39] systems, with several proposals extending the technique to the quantum regime [40, 41, 42], including approaches utilizing neural networks [43]. However, a specific quantum procedure for levitated optomechanics has yet to be fully developed and requires further research.

5. Repeatability of the whole procedure is also important to gather the necessary ensemble statistics and resolve the signature features. The same conditions over repetitions must be ensured to measure the result. This forces one design a protocol to reuse the same particle in each run.

1.4 Thesis overview

In this thesis, we explore experiments with optically levitated nanoparticles aimed at pushing these systems into the quantum regime.

We first examine how external nonlinearities can be introduced into the nanoparticle's motion through feedback control mechanisms. Utilizing real-time position readout, these feedback systems dynamically actuate on the particle, facilitating the controlled introduction of nonlinear interactions.

Next, we investigate the expansion of the nanoparticle's mechanical state via parametric modulation. We analyze how the intrinsic nonlinearity of the trapping potential acts to split the state, thereby generating distinct non-Gaussian features, offering a pathway to exploring quantum state preparation.

Finally, we theoretically address the use of structured light for COM position readout. We demonstrate that specific configurations of the light field can be tailored to avoid providing position information, thereby suppressing decoherence and enabling minimally invasive measurements. This opens avenues for the controlled manipulation of the nanoparticle's quantum state.

2
Optical Trapping

Since this thesis focuses on optical levitation experiments, it is natural to begin with a discussion of the fundamental optical forces that govern the dynamics of levitated particles, along with other key aspects relevant to the behavior of mesoscopic systems. This foundational overview will provide the necessary context for understanding the interaction between light and matter in the regimes explored in the experiments of our work.

2.1
Optical forces

The interaction of light with matter, particularly a spherical object, can be classified into three regimes based on the ratio of the incident wavelength λ to the sphere's radius r and volume $V = \frac{4}{3}\pi r^3$. If the wavelength is much smaller than the particle radius ($\lambda \ll r$) a geometric treatment of optics is possible. If the wavelength is comparable to the particle radius ($\lambda \approx r$) the scattering can be quite complex due to resonances, but the Mie scattering theory that takes into account the vectorial nature of Maxwell equations is a feasible approach. For wavelengths much bigger than the particle radius ($\lambda \gg r$) the Rayleigh scattering description applies.

It is desirable to work in the dipole regime because the dipole interaction primarily couples to the gradient of the electromagnetic field rather than directly to the photon flux, allowing for highly stable three-dimensional trapping. In addition, smaller particles tend to have higher trap frequencies, this means their ground-state energy, $E_{ground} = \hbar\Omega_0/2$, tends to be higher. Higher mechanical frequencies reduce thermal occupation because each phonon carries more energy. At a given thermal energy $k_B T$, fewer phonons are excited, making it easier to reach the quantum regime with suitable cooling techniques. In the following section, we will explore this regime in detail and examine how the restoring force enables optical trapping.

The nanoparticle is modeled as a linear dielectric with refractive index n_p, and permittivity $\epsilon_p = n_p^2$, embedded in a medium with refractive index n_m and permittivity $\epsilon_m = n_m^2$. The relative index of refraction $n_r = n_p/n_m$. When the electromagnetic field interacts with the particle, it induces a local separation of charges, resulting in an electric dipole moment, $\mathbf{P} = \alpha\mathbf{E}$, within the bulk of the particle. The particle's response to the electric field is characterized by its polarizability, α, which we formulate by the Clausius-Mossotti relation,

$$\alpha = 3\epsilon_m V \frac{n_r^2 - 1}{n_r^2 + 2}, \tag{2-1}$$

calculated considering the spherical geometry of the particle. Under these conditions, the particle can be treated as a point-like object, devoid of internal structure, with an effective dipole moment governed by its polarizability. This parameter serves as the key coupling factor between the particle's center-of-mass motion and the electromagnetic field.

From the Lorentz force one can find an expression for the electromagnetic force acting on a point dipole,

$$\mathbf{F} = \alpha\Big(\frac{1}{2}\nabla|\mathbf{E}|^2 + \frac{d}{dt}(\mathbf{E}\times\mathbf{B})\Big). \tag{2-2}$$

2.2 Gradient and Scattering force

Using the Clausius-Mossotti relation (Eq. 2-1) and the relation between the time averaged electric field and intensity $I = cn\epsilon_0|\mathbf{E}|^2/2$. The first term in (Eq. 2-2) takes the form of a gradient seeking force kown as gradient force,

$$\mathbf{F}_{grad} = \frac{1}{2}\alpha\nabla|\mathbf{E}|^2 = \frac{4\pi n r^3}{c}\frac{n_r^2 - 1}{n_r^2 + 2}\nabla I. \tag{2-3}$$

The second term in Eq. 2-2 is the scattering force,

$$\mathbf{F}_{scat} = \alpha\frac{d}{dt}(\mathbf{E}\times\mathbf{B}) = \frac{128\pi^5 r^6}{3c\lambda_0^4}\Big(\frac{n_r^2 - 1}{n_r^2 + 2}\Big)^2 n^5 I\hat{z}. \tag{2-4}$$

On one hand, the gradient force is of significant interest, as it directs the particle towards regions of high light intensity, as shown in Fig. 2.1. In a tightly focused beam, the gradient force generates a three-dimensional restoring force, enabling highly stable trapping with depths well above the noise instabilities caused by the ambient temperature of atmospheric air during the initial particle loading phase.

On the other hand, the scattering force (Eq. 2-4) is non-conservative and leads trap instability making it generally undesirable for optical trapping. Fortunately it's relative importance to the gradient force scales with the third power of the particle radius and is underwhelmed by for small particles as is the case we will be dealing with in this work [44].

2.3 Trapping light field

The gradient force generated by weakly focused beams, only provide transversal trapping [45]. Highly focused laser beams, in contrast, provide the intensity profiles needed for optical trapping in three dimensions [46]. A

Figure 2.1: Charge separation of a polarizable sphere under influence of a homogeneous electric field. If an electric field gradient is present a net force appears.

convenient approximated way to describe such beams, which captures the basic key physical aspects of the problem, arises from the paraxial approximation of the Helmholtz equation, whose fundamental solution is the Gaussian beam. In cylindrical coordinates the Gaussian beam intensity is given by,

$$I(r,z) = I_0\Big(\frac{w_0}{w(z)}\Big)^2 \exp\Big\{(-\frac{2r^2}{w(z)^2})\Big\}. \tag{2-5}$$

Where the waist at the focus is, $\omega_0 = \lambda_m/\pi NA$. The laser wavelength in the medium is, $\lambda_m = \lambda_0/n_m$. The numerical aperture (NA) of the beam relates to the angle of divergence, $NA = n_m \sin(\theta_0) = \sin(w_0/z_r)$, which will be further discussed below. The beam radius spreads according to,

$$\omega(z) = \omega_0\Big[1 + (\frac{z}{z_r})^2\Big]^{1/2}. \tag{2-6}$$

The Rayleigh range, defined as the distance over which the beam radius spreads by a factor of $\sqrt{2}$ is given by, $z_r = \pi\omega_0^2/\lambda_m$.
The experimentally accessible laser power relates to the intensity at the focal plane $I_0 = 2P/\pi w_0^2$.

A depiction of the Gaussian beam intensity, (Eq. 2-5), can be seen as a transversal section in (Fig. 2.2 A) with the beam waist indicated as a solid gray line. The axial section is shown in (Fig. 2.2 B) where the solid gray lines indicates the beam radius (Eq. 2-6). This beam radius is a hyperbole curve and it approaches an asymptotic limit, forming a divergence angle, θ_0, with the optical axis.

The Gaussian beam intensity creates the necessary profile to generate a restoring force that confines the particle, with the resulting gradient force forming a trapping potential,

$$U(r,z) = -\frac{4\pi n_m R^3}{c}(\frac{m^2-1}{m^2+2})I(r,z). \tag{2-7}$$

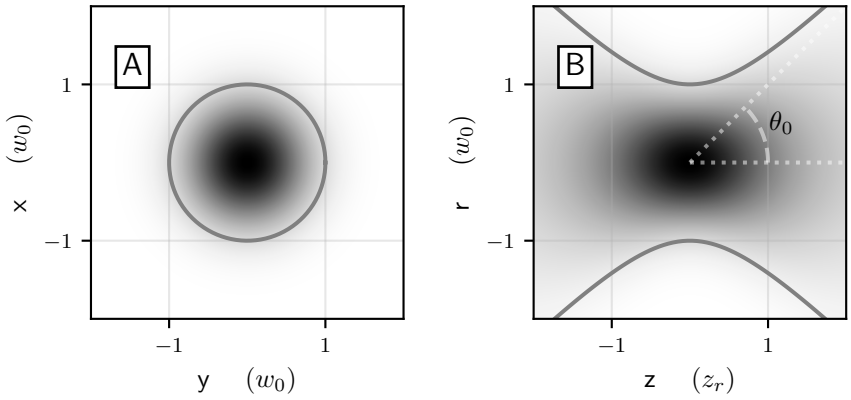

Figure 2.2: Intensity profile of paraxial Gaussian beam Eq. (2-5). Panel A: transversal section at $z = 0$ with solid red circle indicating beam waist w_0, which encloses the region containing the majority of the beam's power. Panel B: axial section with beam radius $w(z)$ indicated by solid red hyperbole Eq. (2-6).

Taylor expansion of the intensity (Eq. 2-5) is possible, and is a specially reliable approximation for particles oscillating with low amplitudes. To do that we can first expand the inverse beam radius squared,

$$\frac{1}{\omega(z)^2} = \frac{1}{\omega_0^2}\frac{z_r^2}{z_r^2+z^2} = \frac{1}{\omega_0^2}\Big(1-\frac{z^2}{z_r^2}\Big) + \mathcal{O}(z^4). \tag{2-8}$$

Expanding also the exponential term,

$$\exp\Big\{(-\frac{2r^2}{w(z)^2})\Big\} = 1 - \frac{2r^2}{w(z)^2} + \mathcal{O}(r^4) = 1 - \frac{2r^2}{w_0^2} + \mathcal{O}(r^4, z^4, r^2z^2), \tag{2-9}$$

Allow us to find the optical potential to second order in r and z.

$$\frac{U(r,z)}{U_0} = 1 - \frac{2r^2}{\omega_0^2} - \frac{z^2}{z_r^2} + \mathcal{O}(r^4, z^4, r^2z^2). \tag{2-10}$$

Where we have defined the potential depth as,

$$U_0 = -\frac{4\pi n_m R^3}{c}(\frac{m^2-1}{m^2+2})I_0. \tag{2-11}$$

By comparing the approximated optical potential (Eq. 2-10) with the elastic potential energy of a generic harmonic oscillator, $U_{har}(x) = kx^2/2$, we can determine that the optomechanical spring constants for the levitated particle are $k_r = 4U_0r^2/\omega_0^2$ for the transverse direction and $k_z = 2U_0z^2/z_r^2$ for the and axial direction.

This indicates that levitated optomechanics is a system that operates with an adjustable natural frequency of oscillation within a frequency range of 10 kHz to 500 kHz, achieved by selecting the appropriate trapping laser power.

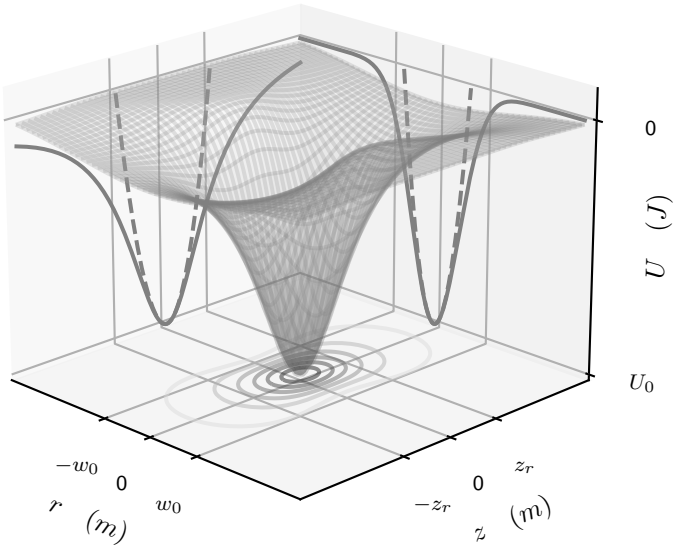

Figure 2.3: The trapping potential for a dipole particle in an optical field formed by a Gaussian intensity profile creates a localized potential well, where the particle experiences forces that confine it near the peak intensity region Eq. (2-7).

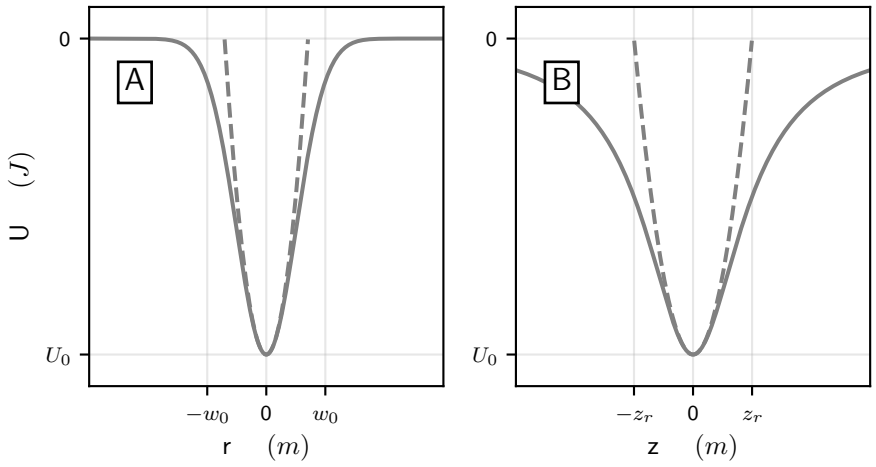

Figure 2.4: **Panel A:** Potential well along the transverse direction ($z = 0$), with the dashed line representing the harmonic approximation. **Panel B:** Potential well along the axial direction ($r = 0$), with the dashed line illustrating the harmonic approximation.

2.4 Gas damping

The damping rate, $\Gamma_m = \Gamma/m$, which governs the attenuation of oscillations, plays a crucial role in levitated nanoparticle dynamics. The primary source of damping is collisions with gas molecules, which are linearly depen-

dent on the pressure, P, up to pressures as low as 10^{-7} mbar, where photon recoil heating becomes the dominant damping mechanism [47]. In the pressure regime dominated by gas collisions, the damping rate can be expressed as [48]

$$\Gamma_m = \frac{64r^2}{3m\overline{v}_{gas}}P, \tag{2-12}$$

with $\overline{v}_{gas}$ the mean thermal velocity of the gas molecules at room temperature.

2.5 Particle dymanics

Focusing on motion along a single spatial direction, x, y, or z, collectively denoted as q, one can write down the equation of motion,

$$\ddot{q}(t) + \Gamma_m \dot{q}(t) + \omega_0^2 q = \frac{F_{\text{drive}}(t)}{m}. \tag{2-13}$$

Let's begin analysing the levitated particle dynamics by first studying the one dimensional harmonic oscillator driven by a force, $F_{drive}(t)$, in the frequency domain. To do that we need to consider the the Fourier transform of position and driving force,

$$\tilde{q}(\omega) = \int_{-\infty}^{\infty} q(t)e^{-i\omega t}\,dt, \quad \tilde{\mathcal{F}}_{\text{drive}}(\omega) = \int_{-\infty}^{\infty} F_{\text{drive}}(t)e^{-i\omega t}\,dt. \tag{2-14}$$

Any arbitrary periodic driving force can be expressed as a linear combination of sinusoidal functions. Therefore, studying a single sinusoidal input is essential for understanding the dynamics of oscillatory systems, as it captures the system's response to more complex forces.
The Fourier transform of the harmonic oscillator equation of motion,

$$-\omega^2\tilde{q}(\omega) - i\omega\Gamma_m\tilde{q}(\omega) + \omega_0^2\tilde{q} = \tilde{\mathcal{F}}_{drive}(\omega), \tag{2-15}$$

allows it's mechanical susceptibility,

$$H(\omega) = \frac{1/m}{\omega_0^2 - \omega^2 + i\gamma\omega}, \tag{2-16}$$

to be defined. This concept helps to understand how the oscillator reacts to an external driving depending on it's frequency, $\tilde{q}(\omega) = H(\omega)\tilde{\mathcal{F}}_{\text{drive}}(\omega)$. The mechanical susceptibility plot for amplitude and phase can be seen in (Fig. 2.5).

2.6 Fluctuating force

In high vacuum conditions the dominant driving mechanism for optical levitation arises from gas molecules collisions, which makes impossible for the

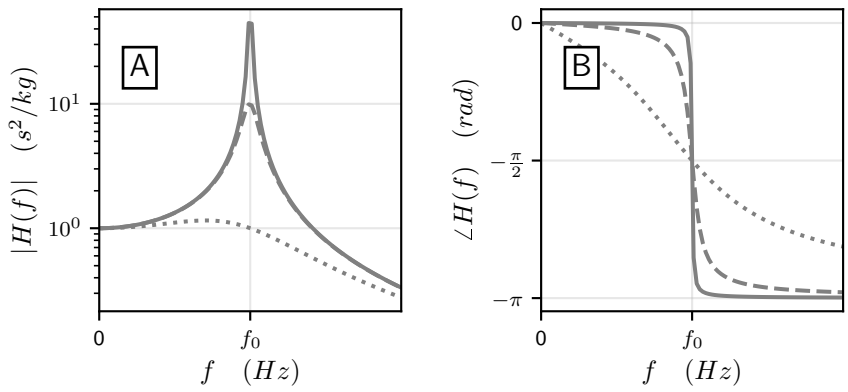

Figure 2.5: Transfer function of the harmonic oscillator for three different values of quality factor, $Q = \omega_0/\Gamma_m$, as $Q = 1$, 10 and 100 as doted, dashed and solid lines respectively.(2-16). Panel A: Absolute value of $H(f)$ shows a an enhanced response for driving frequencies near the natural frequency of the oscillator. Panel B: relative phase of oscillator in relation to driving force. In the DC limit, $f \to 0$, the oscillator behaves as a dynamometer. for resonant drives, $f = f_0$, the oscillator lags behind by 90°. High quality factors produce sharper transitions on phase response.

particle's movement to remain completely still. Rather the particle will always be subjected to noisy Brownian motion due to interaction with its surrounding medium, constantly driving the system. The immense number of collisions, makes a detailed description of each interaction computationally impractical. Therefore, it is more effective to focus on large-scale behavior by reducing the resolution at the microscopic level. In this context, we model the driving as a time-dependent fluctuating force. By doing so, (Eq.2-13) transforms into a type of stochastic differential equation, known as the Langevin equation (Eq.2-17), which captures the interplay between deterministic forces and random fluctuations and is well-suited for describing the classical dynamics of an optically levitated nanoparticle.

$$m\ddot{\vec{r}}(t) = -m\Gamma_m\dot{\vec{r}}(t) + \vec{F}(\vec{r}(t)) + \mathcal{F}_{fluct}(t), \tag{2-17}$$

2.7 Power spectral density

In general terms, the PSD of a signal $X(t)$ is defined as

$$S_{XX}(\omega) = \lim_{T\to\infty} \mathbb{E}\left[\frac{1}{2T}\left|X_T(\omega)\right|^2\right]. \tag{2-18}$$

where the finite-time Fourier transform of the process is given by

$$X_T(\omega) = \int_{-T}^{T} X(t)e^{-i\omega t}dt. \tag{2-19}$$

Substituting this into Eq. (2-18), we obtain

$$S_{XX}(\omega) = \lim_{T\to\infty} \frac{1}{2T}\mathbb{E}\left[\int_{-T}^{T}\int_{-T}^{T} X(t)X^*(t')e^{-i\omega(t-t')}dtdt'\right]. \tag{2-20}$$

The PSD can thus be identified as the Fourier transform of the function

$$R_X(t,t') = \mathbb{E}\left[X(t)X^*(t')\right], \tag{2-21}$$

known as the autocorrelation function.

For wide-sense stationary (WSS) processes, the autocorrelation function depends only on the time difference $\tau = t - t'$, rather than on the absolute time, leading to

$$S_X(\omega) = \lim_{T\to\infty} \frac{1}{2T}\int_{-T}^{T}\int_{-T}^{T} R_X(\tau)e^{-i\omega\tau}dtdt'. \tag{2-22}$$

Since $R_X(\tau)$ depends only on τ, we introduce the midpoint variable $u = (t + t\prime)/2$. The Jacobian of this transformation gives $dtdt\prime = dud\tau$, with integration limits $u \in [-T, T]$ and $\tau \in [-2T, 2T]$. Integrating over u contributes a factor of $2T$, canceling the prefactor $1/(2T)$, leaving

$$S_X(\omega) = \int_{-\infty}^{\infty} R_X(\tau)e^{-i\omega\tau}d\tau. \tag{2-23}$$

This result is known as the Wiener-Khinchin theorem.

The coupling of the levitated particle to the thermal bath implies that it exhibits a thermal state of motion, necessitating a statistical description. The position variance serves as an effective parameter to characterize the thermal energetics of the system, and the power spectral density (PSD) provides a suitable framework for its analysis. To understand the PSD of the dynamical variable q , introduced in Eq.(2-13), one can invoke the concept of the transfer function (Eq.(2-16)) and recognize that the thermal energy of the bath excites all available degrees of freedom of the system, leading to

$$S_{qq}(\omega) = |H(\omega)|^2\langle|\tilde{\mathcal{F}}\text{fluct}(\omega)|^2\rangle = \frac{1}{m^2}\frac{\langle|\tilde{\mathcal{F}}_{\text{fluct}}(\omega)|^2\rangle}{(\omega_0^2-\omega^2)^2+\Gamma_m^2\omega^2}, \tag{2-24}$$

which describes the distribution of variance density across infinitesimal frequency bands.

Since the fluctuating force is modeled as white noise, it contributes an equal amount of fluctuation power at each frequency. By the residue theorem the PSD (Eq. 2-24) can be integrated over all frequencies,

$$\frac{\langle|\tilde{\mathcal{F}}_{fluct}(\omega)|^2\rangle}{m^2}\int_{-\infty}^{\infty}\frac{d\omega}{(\omega_0^2-\omega^2)^2+\Gamma_m^2\omega^2} = \frac{\langle|\tilde{\mathcal{F}}_{fluct}(\omega)|^2\rangle}{m^2}\frac{\pi}{\Gamma_m\omega_0^2}. \tag{2-25}$$

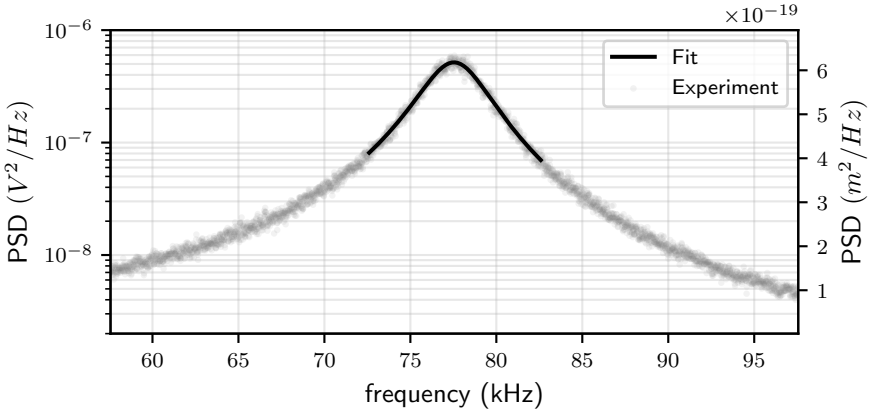

Figure 2.6: **Calibration** PSD of experimental data and fitted theoretical curve. $\omega_0/2\pi = 77.59$ kHz Levitated particle at 5 mbar results in $\Gamma_m/2\pi = 4.12$ kHz. The right y-axis expresses the PSD in meters. Such conversion is possible by using the equipartition theorem and the conversion factor is $\gamma_{m/V} = 831.5$ nm/V.

Using that $\omega_0^2 = k/m$, and that $\int_{-\infty}^{\infty} S_{qq}^{th}(\omega)\, d\omega = \langle x^2(t)\rangle$, the equipartition theorem implies that the thermal force white noise spectrum has a strength that depends on the damping rate,

$$\langle |\tilde{\mathcal{F}}_{fluct}(\omega)|^2 \rangle = \frac{m k_B T \gamma}{\pi}. \tag{2-26}$$

This result is known as the fluctuation-dissipation theorem [49] and can be seem graphically in (Fig. 2.7). Here, k_B is the Boltzmann's constant and T the temperature of the gas surrounding the oscillating particle [49], while $\eta(t)$ is a zero-mean, delta-correlated Gaussian white noise such that

$$\mathbb{E}[\eta(t)\eta(t')] = \delta(t - t'). \tag{2-27}$$

By considering only the experimentally relevant positive frequencies, $\omega > 0$, we obtain the one-sided PSD.

$$S_{qq}(\omega) = \frac{k_B T}{m\pi} \frac{\Gamma_m}{(\omega_0^2 - \omega^2)^2 + \Gamma_m^2 \omega^2}. \tag{2-28}$$

Allowing for the characterization of the trap's parameters as illustrated (Fig. 2.6) [50, 13]. The (Eq. 2-28) has units of meters; however, experimentally acquired data are read with a photo-detector and recorded with an oscilloscope as Volts. A calibration parameter, $\gamma_{m/V}$, is introduced to convert measured voltages into physically meaningful displacements in meters.

2.8 Euler-Maruyama numerical solver for Langevin dynamics

The Langevin equation can be integrated numerically. The time dependence on the noise is non trivial. Since the thermal force is modeled as white

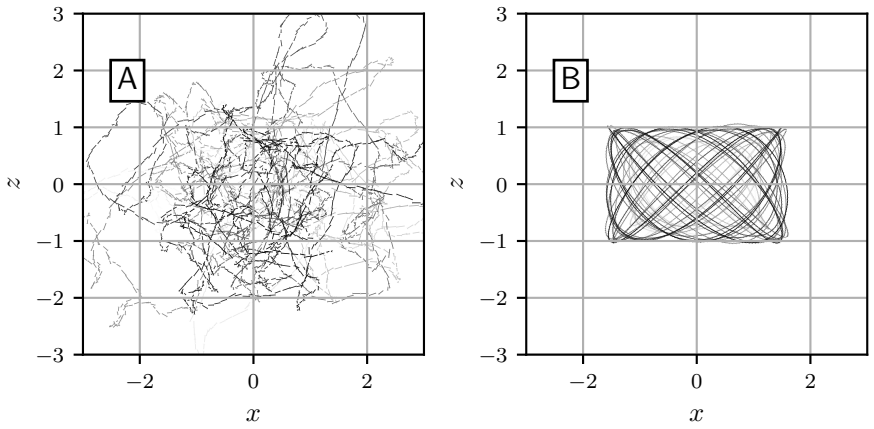

Figure 2.7: **Fluctuation-dissipation** The fluctuation-dissipation term links the strength of fluctuation force with the damping rate. The random nature of the collision does not only provide damping Γ_m, but also a stochastic force F_{fluc}, which thermalizes the energy of the nanoparticle. The fluctuation-dissipation theorem links the damping rate intimately to the strength of the stochastic force, $F_{fluyc}(t) = \sqrt{2m\Gamma_m K_B T_0}\xi(t)$ *Panel A*: Particle trajectory in 2D with high damping ratio. *Panel B*: Particle trajectory in 2D with low damping ratio.

noise its correlation is a delta function,

$$\mathbb{E}[\eta_i(t)\eta_j(t')] = \delta_{ij}\delta(t-t'). \tag{2-29}$$

Thus, for correct dimensions the random force increment in a time step, Δt, has to scale as $\sqrt{\Delta t}$. The Wiener increments of noise, $\Delta W_n = W_{\tau_{n+1}} - W_{\tau_n} = \mathcal{N}(0, \sqrt{\Delta t})$ is a normally distributed random variable with variance Δt that is used for discretized numerical integration scheme.

$$\dot{q}_{n+1} = \dot{q}_n + \Gamma_m \dot{q}_n \Delta t + \omega_0^2 q_n \Delta t + \sqrt{2\Gamma k_B T_{\text{eff}}/m^2}\Delta W_n, \tag{2-30}$$

$$q_{n+1} = q_n + \dot{q}_n \Delta t \tag{2-31}$$

This concludes the concise overview of the toolbox required to understand the experimental discussions presented in the following sections.

3
Perturbative nonlinear feedback forces for optical levitation experiments

In this chapter, we explore the influence of an external, non-linear force of electrical origin on the motion of a levitated particle. This force is applied through time-dependent, spatially uniform electric fields acting on a charged particle. A feedback loop processes the particle's position signal, generating an effective tunable position-dependent nonlinear force.

The theoretical predictions concerning the impact of perturbative nonlinear forces on the spectrum of tweezed nanoparticles, as outlined in [51], are experimentally validated here, with a particular focus on the underdamped regime. Specifically, we confirm spectral corrections induced by tunable Duffing nonlinearity perturbations. By adjusting the strength of the Duffing nonlinearity, as seen in (Fig. 3.1), we examine its influence on the power spectral density (PSD). Both spectral broadening and a shift in the center frequency are expected, but we focus primarily on the frequency shift, as it represents the dominant first-order effect. Our experimental results show quantitative agreement with the theoretical predictions in [51], and the findings are further detailed in [52].

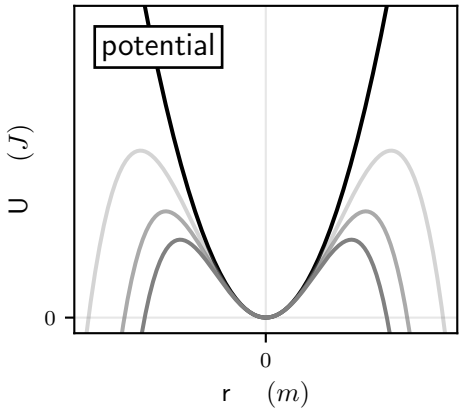

Figure 3.1: A harmonic potential distorted by the inclusion of a Duffing nonlinearity exhibits significant changes in its shape. As the strength of the nonlinearity increases, the potential broadens, deviating from the parabolic profile characteristic of purely harmonic systems. This widening reflects the influence of the quartic term in the Duffing potential, which introduces anharmonic effects that behaves as an effective softening of the harmonic potential.

In the presence of nonlinear potential landscapes, referred to here as nonlinear optical tweezers, the quantitative statistical description of stochastic

particle motion becomes significantly more complex due to the involvement of nonlinear stochastic differential equations. While in harmonic approximations of optical tweezers the mechanical susceptibility of the oscillator can be derived using the Fourier transform of the Langevin equation of motion (Eq. 2-24), this approach fails in nonlinear potential landscapes where the Fourier transform is no longer applicable. To make quantitative predictions about the statistical correlators of the trapped particle's motion in such cases, we can instead rely on perturbation theory [53]. This method, developed using stochastic path integrals [51], enables the computation of corrections to the statistical moments of particle motion as Gaussian integrals, including the position power spectrum, which is widely used in experimental physics. The purpose of this work is to experimentally validate these theoretical methods.

A systematic investigation of nonlinearity effects using Gaussian beam tweezers in the dipole regime is challenging, as both the linear and nonlinear spring constants scale proportionally with trapping power, making independent variation difficult [54]. Although adjusting the numerical aperture (NA) of the focusing element could, in principle, modulate the relative contributions of the linear and nonlinear components, practical control over the NA is constrained. To address this, we introduce effective feedback-controlled potential landscapes, allowing us to impose nonlinear, position-dependent forces on a levitated nanosphere. This nonlinearity is realized via electric feedback, and we characterize its influence on the particle's dynamics.

This discussion is organized as follows. In the next section, we briefly review the perturbation theory for computing corrections to the correlation functions of a trapped particle under the influence of a nonlinear force, and generalize it to include the effect of delayed forces. Since we deal with artificial electric feedback potentials relying on measurements and processing of the trapped particle's position, they imply an inherent delay to the nonlinear force and therefore accounting for the effects of this delay is essential to validating the methods of [51]. We then describe the experimental setup used to generate nonlinear potential landscapes through electric feedback on the particle and numerically compute the effects of delay, showing that within the range of parameters employed in our experiment they are negligible. We implement a cubic force (quartic potential) on the particle and finally verify the perturbation theory by comparing the predicted center frequency of the position power spectral density with experimental results. We conclude with a brief discussion on the applications of artificial nonlinear forces to levitated optomechanics experiments.

3.1 Theory

This section provides a concise overview of the theoretical framework underpinning this experiment, as presented in Ref. [51].

3.1.1 Formulation of the perturbation theory

We model the stochastic motion of a particle in a fluid at thermal equilibrium at temperature T_{eff} and under a force field $\vec{F}(\vec{r})$ using the Langevin equation,

$$\ddot{\vec{r}}(t) = -\Gamma_m \dot{\vec{r}}(t) + \vec{F}(\vec{r}(t))/m + \sqrt{C}\vec{\eta}(t), \tag{3-1}$$

where m is the particle's mass, $\Gamma_m = \Gamma/m$, $C = 2\Gamma k_B T_{\text{eff}}/m^2$ with Γ the drag coefficient and $\vec{\eta}(t)$ is isotropic Gaussian white noise, whose components satisfy

$$\mathbb{E}[\eta_i(t)\eta_j(t')] = \delta_{ij}\delta(t-t'). \tag{3-2}$$

Concentrating in the motion along the longitudinal z-direction, Eq. (3-1) reduces to a one dimensional Langevin equation

$$\ddot{z}(t) = -\Gamma_m \dot{z}(t) + F_z(z(t))/m + \sqrt{C}\eta(t). \tag{3-3}$$

For an approximately linear trapping force perturbed by nonlinear corrections, the steady state position auto-correlation $A(t) \equiv \mathbb{E}[z(t)z(0)]$ can be perturbatively approximated. We next summarize the perturbation theory outlined in [51] and used throughout this work.

Consider the symmetric force acting on the particle,

$$F_z(z) = -m\omega_0^2 z - G_{fb} z^3, \tag{3-4}$$

where the first term accounts for a harmonic optical trap with resonance frequency ω_0 and the second term is a small nonlinear correction, which in the experiment originates from a feedback force on the particle proportional to the *feedback gain* G_{fb} times a nonlinear function of the particle's position. We define the Green function, which comes from the homogeneous equation of the harmonic oscillator,

$$G(t) = \frac{\sin(\Omega\, t)}{\Omega}\ \exp\left(-\frac{\Gamma_m t}{2}\right) H(t), \tag{3-5}$$

where $\Omega = \sqrt{\omega_0^2 - \Gamma_m^2/4}$ and $H(t)$ is the Heaviside step function with $H(t) = 1$ for $t > 0$ and $H(t) = 0$ for $t \leq 0$. We introduce the auxiliary variable (also referred to as the response paths) $\tilde{z}(s)$ and define the Wick sum bracket, $\langle(\cdots)\rangle_0$, that describes the correlation structure of the stochastic process in terms of pairwise contractions dictated by a Green's function:

$$\langle z(t_1)\cdots z(t_n)\tilde{z}(s_1)\cdots\tilde{z}(s_m)\rangle_0 = \delta_{nm}\sum_{\sigma}\prod_{j=1}^{n} G(t_j - s_{\sigma(j)}) \tag{3-6}$$

where the sum goes over all permutations σ of indexes $\{1,\ldots,n\}$. The response variables $\tilde{z}(s)$ can be understood as auxiliary integration variables in a stochastic path integral defining the perturbation theory expansion; we refer to [53, 51] for details on stochastic perturbation methods. Note that the second order correlator is given by the Green function, $\langle z(t)\tilde{z}(s)\rangle_0 = G(t-s)$. The perturbation theory is summarized by the expression for the position auto-correlation function,

$$A(t) \equiv \mathbb{E}[z(t)z(0)] = \langle z(t)z(0)e^{\frac{C}{2}\int\tilde{z}^2(s)ds}e^{\frac{G_{fb}}{m}\int\tilde{z}^3(t')z(t')dt'}\rangle_0, \tag{3-7}$$

where the right-hand side is defined by expanding both exponentials inside the brackets as a power series in C and in G_{fb}/m and interchanging summations and integrations by applying the Wick bracket $\langle(\cdots)\rangle_0$. Note that only brackets with an equal number of z and $\tilde{z}$ variables are non-vanishing [53, 51].

The first non-vanishing term in the expansion of Eq. (3-7) is

$$\frac{C}{2}\int\langle z(t)z(0)\tilde{z}^2(s)\rangle_0\, ds = C\int G(t-s)G(-s)ds\ , \tag{3-8}$$

which gives the auto-correlation for the case of a linear force $F_z(x) = -m\omega_0^2 z$,

$$A(t)_{(G_{fb}=0)} = \frac{Ce^{-\Gamma_m|t|/2}(2\Omega\cos\Omega|t| + \Gamma_m\sin\Omega|t|)}{\Gamma_m\Omega(\Gamma_m^2+4\Omega^2)}. \tag{3-9}$$

The leading order correction in the feedback gain reads,

$$\Delta A(t) \equiv \frac{C^2G_{fb}}{8m}\int\langle\tilde{z}^2(s_1)\tilde{z}^2(s_2)\tilde{z}(t_1)z^3(t_1)z(t)z(0)\rangle_0\, ds_1ds_2dt_1. \tag{3-10}$$

Expanding the brackets using (3-6) would produce a sum with $5! = 120$ terms, but many of these vanish since $\langle\tilde{z}(t_1)z(t_1)\rangle = G(0) = 0$. Moreover, by symmetry of the integration variables s_1 and s_2, the contribution to the integral of the non-vanishing terms is equal to the contribution of $G(t-t_1)G(-s_1)G(t_1-s_1)G^2(t_1-s_2)$ or $G(-t_1)G(t-s_1)G(t_1-s_1)G^2(t_1-s_2)$. Therefore, the integral in (3-10) is computed by integrating these two terms over t_1, s_1, s_2 and multiplying both integrals by a multiplicity factor $2^3(3!) = 48$. We note that a diagrammatic expansion can be employed to organize non-vanishing terms in the Wick sum; for more details we refer to [51].

From the auto-correlation function perturbation ΔA (Eq. 3-10) we can obtain the corrected power spectral density (PSD) of the particle motion by taking the Fourier transform. We obtain the PSD correction [51],

$$\Delta S = \frac{3G_{fb}C^2}{\Gamma_m\omega_0^2}\frac{\omega^2-\omega_0^2}{[\Gamma_m^2\omega^2+(\omega^2-\omega_0^2)^2]^2} \tag{3-11}$$

Note the total PSD, $S_{(G_{fb}=0)}+\Delta S$, can be approximated to linear order in G_{fb} as the PSD of a linear system with a frequency shift $\Delta\Omega$,

$$\frac{C}{\Gamma_m^2\omega^2+[\omega^2-(\omega_0+\Delta\Omega)^2]^2} \approx \frac{C}{\Gamma_m^2\omega^2+(\omega^2-\omega_0^2)^2} + 4C\omega_0\Delta\Omega\frac{\omega^2-\omega_0^2}{[\Gamma_m^2\omega^2+(\omega^2-\omega_0^2)^2]^2}, \quad (3\text{-}12)$$

Comparing the first order correction in Eq. (3-12) with the correction in Eq. (3-11), we conclude that the nonlinearity causes a frequency shift given by:

$$\frac{\Delta\Omega}{2\pi}=\frac{3k_bT_{\text{eff}}}{4\pi m^2\omega_0^3}G_{fb}\equiv\kappa G_{fb}. \quad (3\text{-}13)$$

We see that effectively, the nonlinear perturbation manifests as a shift in the PSD central frequency scaling linearly with the feedback gain G_{fb} and with a slope given by the constant κ. This is valid for small G_{fb},

$$G_{fb}\ll\frac{m^2\omega_0^4}{2k_bT_{\text{eff}}}. \quad (3\text{-}14)$$

The right-hand side of (3-14) can be used to delimit the validity region of perturbation theory. The shift $\Delta\Omega$ in the central frequency of the PSD is the experimental signature which we use as an indicator of the effect of nonlinear perturbations. It is worth noticing that the shift described by (3-13) also includes intrinsic nonlinearities of the tweezer, which arise due to anharmonicities of the trapping potential [48]. Note, however, that only relative shifts to the original resonance frequency (with the cubic feedback off but in presence of the intrinsic nonlinearities) are measured. Thus, our experiment is not sensitive to the intrinsic anharmonicities of the trap, but only to those effected by the cubic feedback.

3.1.2 Delayed nonlinearities

In addition to nonlinear force perturbations, we will also investigate delayed forces. Feedback forces generated artificially will inherently experience electronic delays. It is known that delayed forces may lead to cooling or heating in harmonic traps. Accounting for the effects of such delays in perturbation theory allows us to understand the limits of validity of Eq. (3-7) for modelling the artificial feedback forces. More broadly, understanding the role of delays might also enable the study of perturbative nonlinear non-Markovian stochastic dynamics [55].

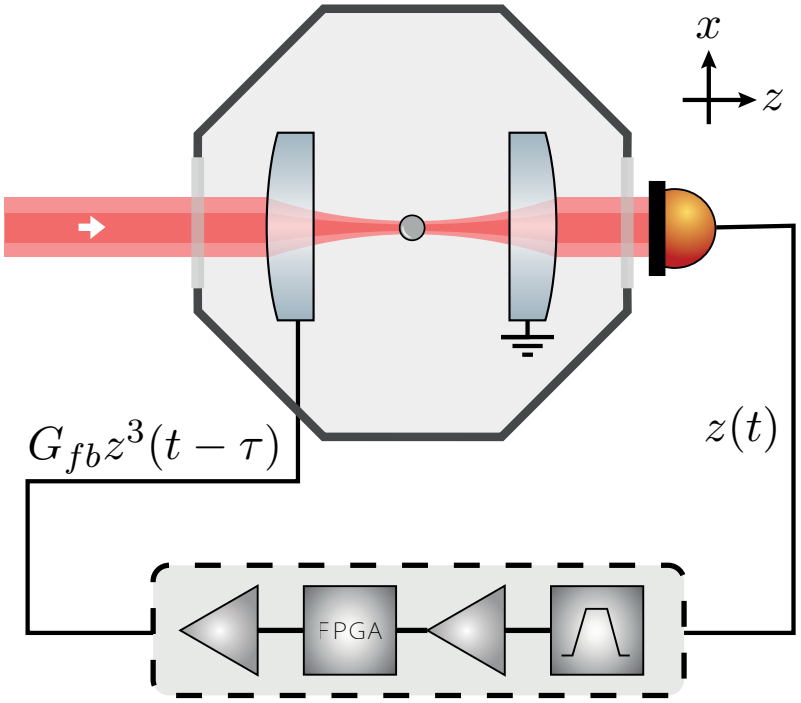

Figure 3.2: **Top view of experimental setup**. A silica nanoparticle is trapped by an optical tweezer in vacuum. The forward scattered light is collected and sent to a photodiode, producing a signal proportional to the particle's axial coordinate, $z(t)$. An FPGA processes the signal to produce a voltage that induces a force on the trapped particle proportional to $z^3(t-\tau)$. Amplification prior to and after the FPGA enhance the maximum resolution of its analog-to-digital converter, enabling the exploration of a broader range of values for the applied electrical force. The x-direction pictured in the scheme is parallel to the optical table.

We consider the generalized Langevin equation,

$$\ddot{z}(t) = -\Gamma_m \dot{z}(t) - \omega_0^2 z(t) - \frac{G_{fb}}{m} z^3(t-\tau) + \sqrt{C}\,\eta(t), \tag{3-15}$$

where $\tau > 0$ is a fixed (constant) time delay.

The perturbation expansion for $\tau = 0$ (Eq. (3-7)) can then be generalized to

$$A(t,\tau) \equiv \mathbb{E}[z(t)z(0)] = \langle z(t)z(0) e^{\frac{C}{2}\int \tilde{z}^2(s)ds} e^{\frac{G_{fb}}{m}\int \tilde{z}(t')z^3(t'-\tau)dt'} \rangle_0. \tag{3-16}$$

Expanding the exponentials in power series and using the Wick sum as defined in (3-6), the leading correction to the auto-correlation function (3-9)

is given by the following integrals,

$$\begin{aligned}\Delta A(t,\tau) \propto & \\ &\int G(t-t_1)G(-s_1)G(t_1-s_1-\tau)G^2(t_1-s_2-\tau)dt_1ds_1ds_2 \\ &+\int G(-t_1)G(t-s_1)G(t_1-s_1-\tau)G^2(t_1-s_2-\tau)dt_1ds_1ds_2\ . \quad (3\text{-}17)\end{aligned}$$

We note both integrals are multiplied by the constant $3G_{fb}C^2/m$, which we omit to avoid cluttering the notation. Evaluating the integrals leads to the corrected auto-correlation function to first order in the perturbation,

$$\begin{aligned}A(t,\tau) \;=\; & \frac{Ce^{-\Gamma_m|t|/2}(2\Omega\cos\Omega|t| + \Gamma_m\sin\Omega|t|)}{\Gamma_m\Omega(\Gamma_m^2+4\Omega^2)} \\ &+\frac{3C^2G_{fb}e^{-\Gamma_m|t|/2}}{64m\Gamma_m^3\Omega^4\omega_0^6}\Big\{e^{\Gamma_m\tau/2}[8\Gamma_m\Omega^4 - 4\omega_0^2\Gamma_m^2\Omega^2(|t|-\tau)]\cos(\Omega(|t|-\tau)) \\ &+e^{\Gamma_m\tau/2}[8\Gamma_m\Omega^3\omega_0^2(|t|-\tau) + 8\Omega^5 + 4\Gamma_m^2\omega_0^2\Omega + 6\Gamma_m^2\Omega^3]\sin(\Omega(|t|-\tau)) \\ &+e^{-\Gamma_m\tau/2}[\Omega^2(2\Gamma_m^2\Omega - 8\Omega^3)\sin(\Omega(|t|+\tau)) + 8\Gamma_m\Omega^4\cos(\Omega(|t|+\tau))]\Big\} \\ &+\mathcal{O}(G_{fb}^2, C^3),\end{aligned}$$

The quantity $A(0,\tau)$ can be experimentally obtained from the area under the PSD of the particle's motion, which in turn can be related to the mean occupation number of the mechanical modes. In what follows, we use these expressions to account for the effects of delay in the artificially generated nonlinear forces, and to show that perturbation theory in the absence of delay provides a good approximation to current experiments.

3.2 Experiment

A simplified schematic of the experimental setup is shown in Figure 3.2. A CW laser at 780 nm (Toptica DL-Pro) is amplified using a tapered amplifier (Toptica BoosTa) producing up to 1.5 W at the output of a single mode fiber, yielding a high quality Gaussian beam. The beam is expanded to overfill an aspheric lens of numerical aperture NA = 0.77 (LightPath 355330) mounted inside a vacuum chamber, which provides a tightly focused Gaussian beam to form the optical trap. A solution of silica spheres of diameter $2R = 143$ nm (MicroParticles GmbH) is mono-dispersed in ethanol and delivered into the optical trap using a nebulizer. Once a single particle is trapped, the pressure

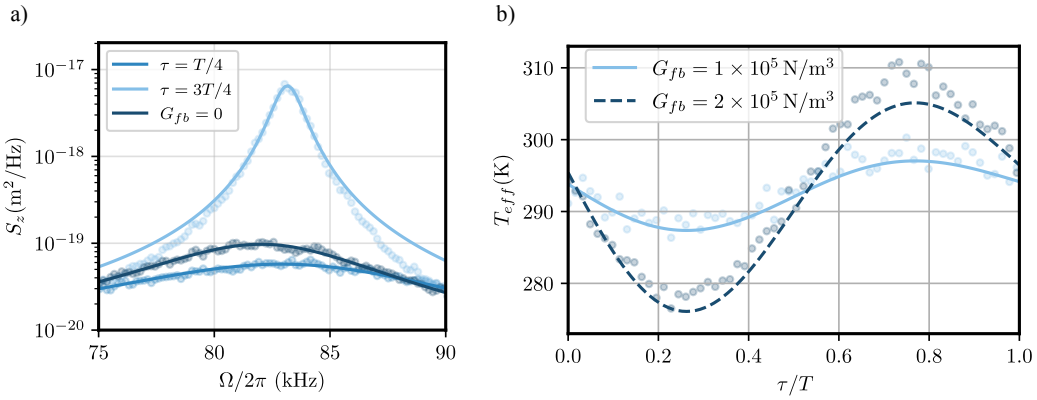

Figure 3.3: Effect of a delayed nonlinearity. a) Longitudinal position PSDs for the reference measurement (dark blue) in comparison to cubic feedback forces at a gain of $G_{fb} = 5.31 \times 10^6\,\mathrm{N/m}^3$ and delays of $\tau = T/4$ (bright blue) and $\tau = 3T/4$ (middle blue). Here, T represents the period of the particle motion along the longitudinal direction. These comparisons reveal how the introduction of a delayed cubic force can either cool or heat the particle motion. b) Numerically simulated effective temperature T_{eff} of particle motion as a function of the delay in the cubic feedback force, displaying cooling and heating in accordance to the predictions of nonlinear delayed perturbation theory described in Sec. 3.1.2. With this analysis, we conclude that the electronic delay present in our experiment, measured to be $\tau/T = 0.042 \pm 0.006$, can be safely neglected.

in the chamber is reduced to 10 mbar. The trapped particle's axial center-of-mass (COM) motion, $z(t)$, is recorded by collecting forward scattered light with an aspheric lens of numerical aperture NA = 0.50, and directing it to a photodiode (Thorlabs PDA100A2), generating an electric signal proportional to $z(t)$.

The signal from the detector is sent to a wide band-pass filter, amplified and then input into an FPGA. The FPGA introduces a tunable delay, raises the signal to the third power and multiplies it by a tunable gain. The output signal is then amplified once again and applied to the mount of the trapping lens, producing a voltage difference with respect to the mount of the collection lens, which is grounded. This generates an electric force at the particle position given by $G_{fb}z^3(t-\tau)$, where τ is the total delay introduced by the electronics and G_{fb} is the overall feedback gain. For more details on the generated electric field and electronics, see Appendices 3.4.1 and 3.4.2.

An artificial quartic potential is generated through a feedback scheme in which a controlled electric voltage is applied to a pair of electrodes connected to the mounts of the trapping and collecting lenses. As explained in Appendix 3.4.1, numerical simulations demonstrate that the electric field generated between the lenses is approximately uniform in the vicinity of the particle's

position and directly proportional to the voltage on the electrodes. The electric voltage applied is proportional to $z(t-\tau)^3$, where τ represents a total delay term. The total delay term is the sum of an intrinsic delay of the setup electronics and a tunable delay term that can be adjusted by an FPGA (Red Pitaya STEMlab board).

In order to establish the feedback mechanism, the signal obtained from the detector is sent to a wide band pass filter and pre-amplified. The FPGA process the amplified signal, generating the non-linear behavior, and transmits it to an amplifier connected to the electrodes. The overall feedback gain, denoted as G_{fb}, is determined by the gains of the two amplifiers, along with an adjustable gain defined within the FPGA. Appendix 3.4.2 gives a comprehensive review of the electronic and software implementation. By feedback of this non-linearity, the described setup enables the creation of an effective and controllable Duffing anharmonicity on top of the existing harmonic optical potential experienced by the levitated particle.

The electronics naturally introduce a delay to the applied position-dependent electric forces, which could lead to deviations from the predictions of the perturbation theory discussed in Sec. 3.1.1. To qualitatively understand the effects of a delayed feedback nonlinear force, we have exaggerated the electronic delay τ applying a cubic force of the form $G_{fb}x^3(t-\tau)$ for $\tau = (2\pi/4\omega_0) = T/4$ and $\tau = 6\pi/4\omega_0 = 3T/4$, and subsequently measured the PSDs of the particle motion along the longitudinal direction. The results can be seen in Figure 3.3a), in comparison to the PSD of the trapped particle in the absence of nonlinear feedback. We see that depending on the delay, the particle undergoes cooling ($\tau = T/4$) or heating ($\tau = 3T/4$). This can be understood as the nonlinear analogue of cold damping, where the delayed feedback signal acquires a force component proportional to the velocity [56, 57, 25].

We can quantify the effect of delay for the case of our experiment using the theory described in Sec. 3.1.2. To do that, we have simulated the particle dynamics under the influence of a delayed feedback cubic force for two different values of the feedback gain G_{fb} within the regime of perturbation theory. For each simulation, we extract the particle motion traces and compute the position variance, from which the effective temperature T_{eff} of the mechanical oscillator can be obtained. The results are plotted in Figure as a function of τ, in comparison to the theoretical prediction given by Eq. . The simulations confirm the qualitative cooling/heating results shown in Figure 3.3 and are in good agreement to the perturbation theory with the inclusion of delay. Notably, for the electronic delay in our experiment, characterized to be $\tau = (0.518 \pm 0.074) \times 10^{-6}\,\text{s}$, we verify that the expected cooling/heating effects

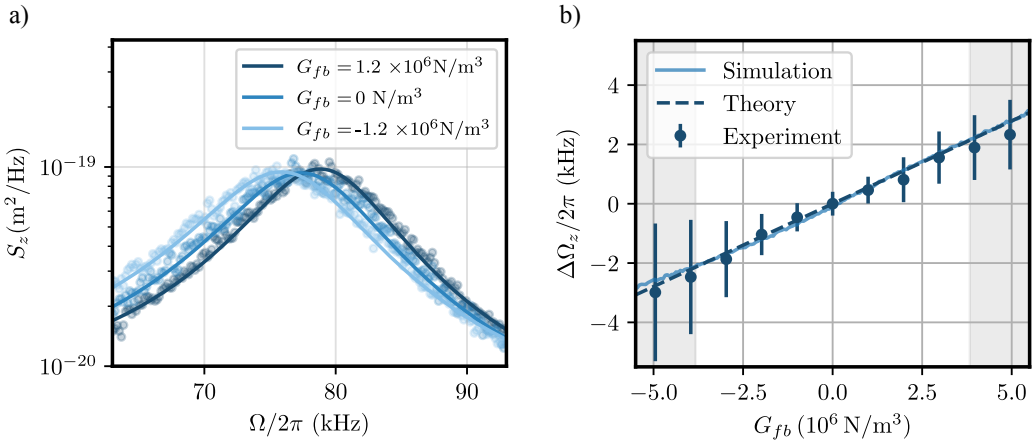

Figure 3.4: Verifying the predictions of perturbation theory: a) PSDs of the trapped particle's longitudinal motion under cubic force, displaying central frequency shifts. The data was taken at 293 K and a pressure of 10 mbar. The reference PSD (middle blue) has a central frequency of 77.8 kHz and a shift of ±1.4 kHz was measured for $G_{fb} = \pm 1.2 \times 10^6\,\mathrm{N/m^3}$. b) Frequency shifts as a function of G_{fb}, verifying the prediction of perturbation theory given by Eq. (3-13) (dashed line). The grey shaded region marks the regime of validity for perturbation theory described in Eq. (3-14). Each point corresponds to 250 seconds of data acquisition at 500 kHz divided into 1000 traces and organized into batches of 5 traces each. All data points were collected using the same nanoparticle.

due to a delayed nonlinear feedback provide a correction to the auto-correlation at the level of 1.10% and are buried within experimental uncertainties. With this analysis we conclude that any effect associated to electronic delay in our experiment is negligible and the perturbation theory in the absence of delay can be used to model the effect of nonlinear perturbations.

We next proceed to verify the perturbation theory as described in Sec. 3.1.1 (without delay, $\tau = 0$). We apply an effective quartic perturbation to the optical potential by acting on the trapped particle with a cubic force which was generated, as previously described, from the position measurement feedback. PSDs of particle motion under the influence of the cubic feedback force with positive and negative feedback gains can be seen in Figure 3.4a). These measurements qualitatively confirm the effect of the cubic force predicted by perturbation theory as a shift in the PSD central frequency. Note the shift depends on the sign of the feedback gain, in accordance to Eq. (3-13), indicating an effective hardening or softening of the optical trap due to the cubic actuation.

To quantitatively compare the frequency shifts with the predictions from perturbation theory, we acquired the longitudinal motion PSD for different values of feedback gain G_{fb}. Note that all parameters going into κ (see Eq.

(3-13)) are obtained from additional setup characterizations, leaving no free parameters for adjusting the theory to the data. For instance, the trap central frequency ω_0 and mechanical damping Γ_m are obtained from Lorentzian fits of the unperturbed PSD, the nanoparticle mass m is calculated from the diameter provided by the manufacturer and from the density of silica, and the applied feedback gain G_{fb} is obtained after the calibration of the detector, electrode and other intermediate electronic elements as described in more detail in Appendix 3.4.2. The particle is taken to be at ambient temperature $T_{eff} = 293\,\mathrm{K}$; note that a $5\,\mathrm{K}$ variation in temperature yields a 2 % variation in theoretical prediction.

Once these characterizations have been performed, the central frequencies of the perturbed PSDs – and consequently the associated shifts – can be obtained by a Lorentzian fit as a function of feedback gain and compared to the theoretical predictions. The result of these measurements is shown in Figure 3.4b), in comparison to the theoretical prediction given in Eq. (3-13) for our experimental parameters.

Good agreement between the data and the theoretical prediction was observed within the perturbation regime, indicated by the non-shaded region of the plot. Note also that outside the regime of perturbation theory (grey shaded regions in Figure 3.4b)), the measured shifts fall systematically slightly bellow the predicted first order correction, consistent with the second-order correction scaling of $\mathcal{O}(G_{fb}^2)$ [51]. Note the error bars in Fig. 3b) are larger for negative feedback in comparison to positive feedback gains. We attribute this to the fact that the intrinsic nonlinearity of the optical trap introduces an effective negative feedback gain ($G_{\mathrm{optical}} \approx 10^6\,\mathrm{N/m^3}$), shifting the regime of validity of perturbation to the right, towards positive gains [48]. Finally, the experimentally obtained angular coefficient κ_e was measured to be

$$\kappa_e = (5.46 \pm 0.10) \times 10^{-4}\,\mathrm{Hz\,m^3\,N^{-1}} \tag{3-18}$$

which compares to the theoretical prediction given the parameters for our experiment,

$$\kappa_t = 5.69 \times 10^{-4}\,\mathrm{Hz\,m^3\,N^{-1}}\ . \tag{3-19}$$

3.3 Conclusions

In conclusion, we have implemented a cubic nonlinear force based on position measurement feedback acting on an underdamped levitated nanopar-

ticle. Effects of the cubic force on the particle's stochastic dynamics have been experimentally studied. In particular, shifts introduced in the particle motion power spectrum due to the presence of the cubic feedback force have been measured. We have verified that these shifts are in accordance to the predictions of the stochastic path integral perturbation theory for nonlinear optical tweezers introduced in [51]. To account for the experimental imperfections due to electronic delay in the feedback, we have also extended the perturbation theory and showed that for feedback schemes currently available in levitated optomechanics experiments the effects of electronic delay can be made negligible.

Nonlinear electric feedback potentials will useful in a number of applications in levitated optomechanics experiments, both in the classical stochastic and quantum regimes. For instance, delayed nonlinear feedback can be used to engineer a non-conservative system with nonlinear damping of the Van der Pol type [58]. Finally, weak measurements of a levitated optomechanical system in a cavity might allow for feedback-induced nonlinear dynamics in the quantum regime [59] – the non-classical version of feedback-induced nonlinear forces.

Building on recent advances in levitated quantum control experiments [26, 25], stronger nonlinear feedback forces could enable the preparation of non-Gaussian states that surpass the intrinsic nonlinearities of optical potentials, as illustrated in Fig. 3.5. While this experiment employed small nonlinearities to remain within the perturbative regime, it is noteworthy that upgrading the electronics to achieve higher amplification gains and kilovolt-range voltages would produce significantly stronger nonlinearities. Such enhancements could be instrumental in preparing non-Gaussian states in the quantum regime, which is discussed in the next chapter of this thesis.

Code and data availability: GitHub. https://github.com/QuantumAdventures/nonlinearity-experiment

3.4 Additional technical discussion

The remainder of this chapter delves into specific technical details of the experimental setup and procedures.

3.4.1 Electric field simulation

One of the experiment's central assumptions is that the electric force acting upon the trapped particle is proportional to the voltage applied to the electrodes and does not depend on its position. Moreover, due to symmetry

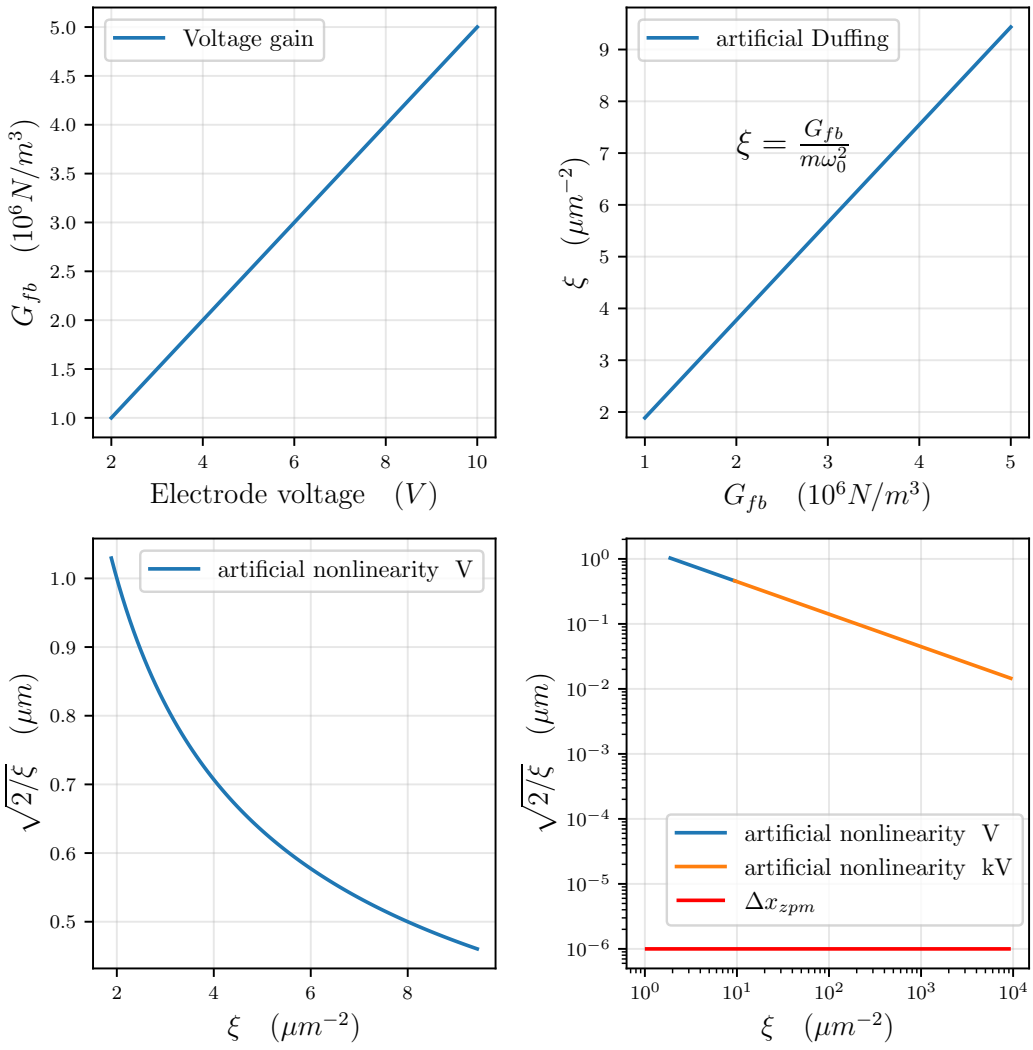

Figure 3.5: Plot illustrating the relationship between the electrode voltage and the nonlinear feedback gain, G_{fb} . The curves demonstrate how our definition of G_{fb} maps onto the broader Duffing parameter, which characterizes the system's nonlinearity. The plot also converts the Duffing parameter into linear position dimensions, facilitating comparisons with characteristic length scales of the motional state, such as the zero-point motion, $z_{\mathrm{zpm}} = \sqrt{\hbar/2m\omega_0}$. The blue curve highlights the regime of small nonlinearity and low voltages within the experimental range, where the system was operated in the perturbative regime. For reference, the orange curve represents higher voltages, achievable with Paul trap electronics in the kilovolt range, which would result into more pronounced nonlinear effects.

around the optical axis, we expect the components of the electric force orthogonal to the optical axis to be negligible. To verify these assumptions, a simulation of the electric potential and electric field generated by the geometry of the optical setup was conducted using COMSOL Multiphysics software (version 5.4).

In Fig. 3.6, the electrical potential between the electrodes is shown for a

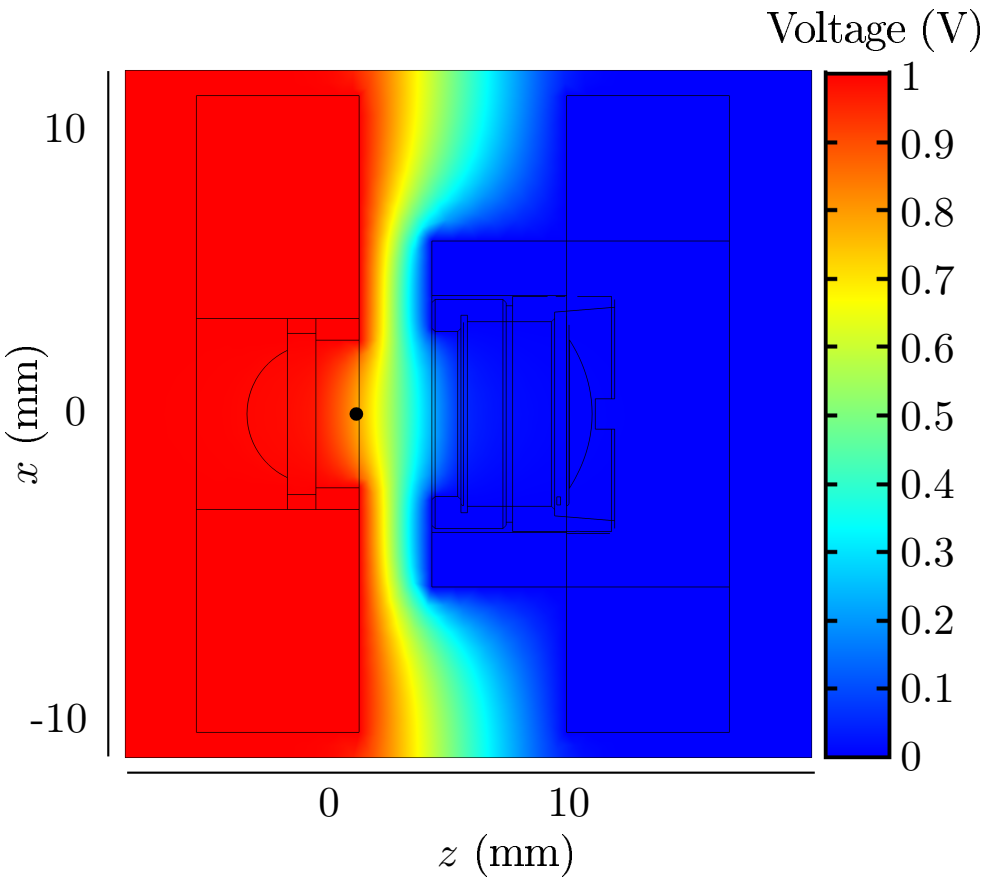

Figure 3.6: Electric potential generated by the electrodes' geometry for a slice in the xz plane passing through the optical axis. The contour shows the internal structure of the optical setup with the black dot marking the average position of the trapped particle, about 1.59 mm away from the flat base of the trapping lens.

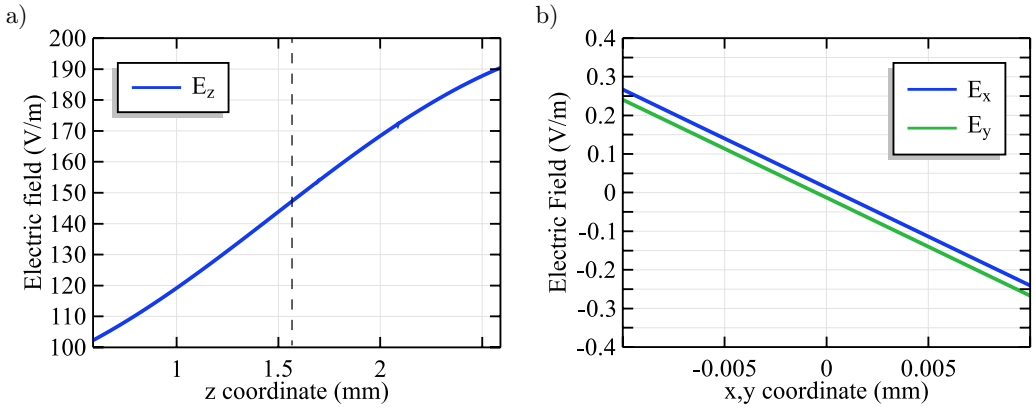

Figure 3.7: (a)-(b) The z and x, y components of the electric field in the vicinity of the trapped particle. The dashed line denotes the average position of the particle.

slice in the xz plane, where the internal contour of the optical setup is displayed for clarity. The left electrode, which contains the trapping lens, is set at 1 V relative to the right one, which holds the collection lens. The black dot denotes

the average position of the trapped particle, 1.59 mm away from the flat base of the aspheric lens. Figures 3.7(a) and 3.7(b) show the electric field components in the vicinity of the particle. Considering an average amplitude of 100 nm for the COM motion, the simulation shows a percent change of roughly 0.01% for the z component of the electric field. Moreover, the x and y components are four to five orders of magnitude smaller than the z component, thus providing a firm foundation for our assumptions.

3.4.2 Electronics

In order to apply the feedback signal, essential steps were undertaken regarding the implementation of an electronic setup aimed at preprocessing the detection signal. First, it was crucial to address a strong DC component present in the signal obtained from the photodetector. To prevent saturation of the Red Pitaya RF input used in the experiment, an analog band-pass filter was implemented for its capability to remove both DC and high-frequency components effectively. While it's common to opt for a Butterworth filter based on the Sallen-Key topology [60], it is important to highlight that this choice introduces an undesirable phase effect.

As demonstrated by simulation results showed in Fig. 3.8 (a), the addition of a Butterworth filter results in a shift of the PSD central frequency, which deviates from the theoretical prediction presented in [51]. To overcome this problem a passive RC filter is used along with a non-inverter amplifier. As evident from Fig. 3.8 (b), the comparison of the Bode diagrams for both topologies illustrates that the passive filter will have minimal impact on the signal phase, while simultaneously maintaining a flat band over a wider frequency range.

The addition of a non-inverting amplifier after the band-pass filter enables the utilization of the full resolution of the ADC on the Red Pitaya board. Furthermore, a second amplifier is incorporated after the FPGA, facilitating the generation of voltage values approximately ten times higher than the board's limit. Upon characterization of both amplifiers, we found that the gains, A_1 and A_2, before and after the FPGA were measured as 11.00 V/V and 11.27 V/V, respectively. These values will be necessary for the calibration of the overall feedback gain G_{fb}, detailed in appendix 3.4.3.

In Fig. 3.8 (c) we illustrate an example of input and output signals of the Red Pitaya. In order to implement the non-linear function, we employed fixed-point arithmetic—a method for representing fractional numbers within a specified range. This approach enables us to execute complex mathematical

operations without suffering from information loss [61], as is often the case with binary representation. Furthermore, it offers straightforward means of extending the code to implement higher-order polynomial functions.

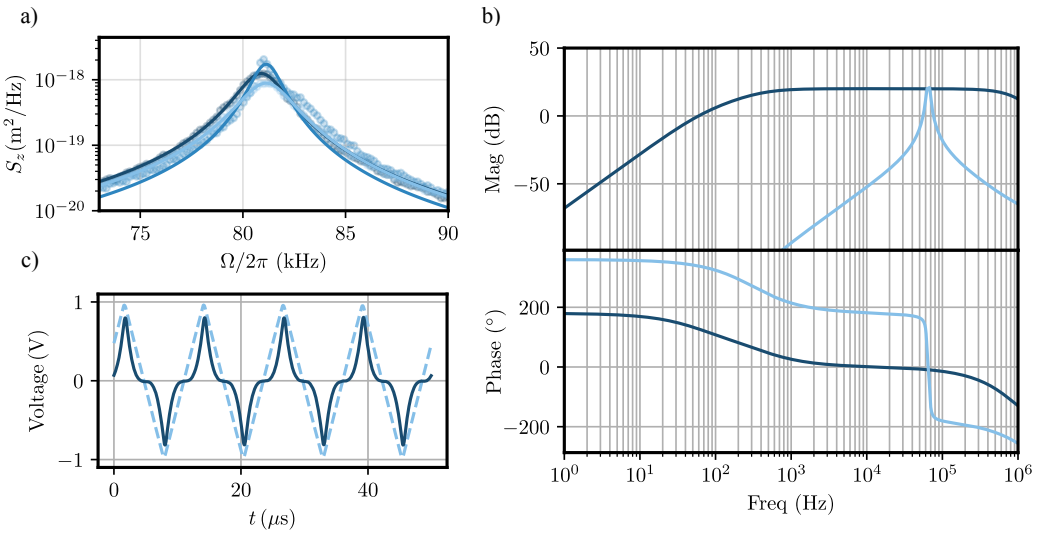

Figure 3.8: Filter design. (a) PSD's obtained from simulations of a tweezed nanoparticle ($\Omega_z/2\pi = 81.5\,\text{kHz}$ and $\Gamma_m = 1.3 \times 10^4\,\text{s}^{-1}$) under the influence of a cubic force. Three scenarios were considered: second-order Butterworth filter with 1 kHz bandwidth (bright blue), 10 kHz bandwidth (middle blue) and, lastly, with no filter (dark blue). (b) Bode diagrams of a highly selective Butterworth filter (bright blue) and of a passive RC filter (dark blue), both circuits were simulated using LTspice XVII. (c) Results from the FPGA program. The dashed line represents the input, which is a triangular wave with a frequency of 81 kHz. The solid line corresponds to the output, which is proportional to the input raised to the third power.

3.4.3 Calibration of applied force

To validate the theoretical predictions outlined in [51], it was necessary to calibrate the overall feedback gain G_{fb}, defined as

$$G_{fb} = C_{NV} A_2 A_d A_1^3 C_{mV}^3, \tag{3-20}$$

where A_1 and A_2 represent the gains originating from the electronic amplifiers, A_d is the tunable digital gain defined within the FPGA, C_{mV} is the calibration factor which converts the measured voltage into corresponding displacement in meters and C_{NV} is the transduction coefficient that establishes the connection between applied voltage across the electrodes and the resulting force applied to the particle; see appendix 3.4.2 for further details.

To calibrate the photodetector, 1000 traces of 0.1 seconds were collected. The PSD of the time traces is fitted by a Lorentizan distribution,

$$S_V(\omega) = \frac{D}{\Gamma_m^2\omega^2 + (\omega^2 - \omega_0^2)^2}, \tag{3-21}$$

where $D = 2\Gamma_m k_B T_{\text{eff}} C_{mV}^2/m$; this take in consideration that $S_V(\omega) = C_{mV}^2 S_z(\omega)$ [50]. This procedure led to a calibration factor of $C_{mV} = (1.504 \pm 0.073) \times 10^4\,\text{V/m}$. After calibration of the detector, we proceed to determine the transduction coefficient, denoted as C_{NV}. To obtain C_{NV}, we subjected the particle to a series of sinusoidal signals with varying amplitudes and measured the particle's response in the position PSD [62]. For a particle subjected to Eq. 4-1, the total PSD $S_z^T(\omega)$ in the presence of an electric drive $F_{el}(t) = F_0\cos(\omega_{dr}t)$ can be expressed as [62],

$$S_z^T(\omega) = S_z(\omega) + S_z^{el}(\omega) = \frac{2\Gamma_m k_B T_{\text{eff}}}{m[(\omega^2 - \omega_0^2)^2 + \Gamma_m^2\omega^2]} + \frac{F_0^2\tau_{el}\,\text{sinc}^2[(\omega - \omega_{dr})\tau_{el}]}{m^2[(\omega^2 - \omega_0^2)^2 + \Gamma_m^2\omega^2]}, \tag{3-22}$$

with $2\tau_{el}$ being the duration of the measure. In Figure 3.9a), we display one of the PSDs used for the electrode calibration. The thin line comes from the electric force, $F_{el}(t)$, and is compared to thermal noise base line as explained in **??**. The resulting calibration curve is presented in Figure 3.9b), which yields a transduction coefficient $C_{NV} = (3.06 \pm 0.13) \times 10^{-15}\,\text{N/m}$. All measurements described in the main text were performed with the same nanoparticle.

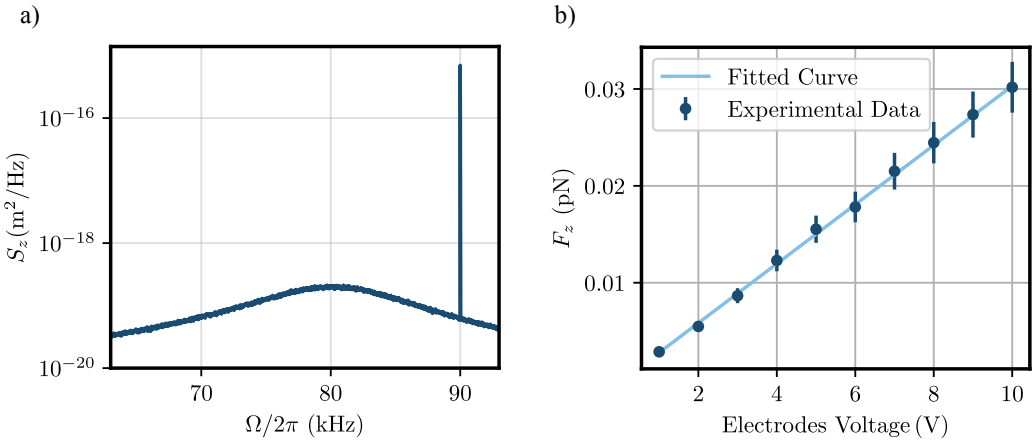

Figure 3.9: Electrode calibration: (a) PSD obtained from a trapped nanoparticle at 10 mbar and $T_{\text{eff}} = 293\,\text{K}$ under the action of a sinusoidal drive (voltage amplitude $V_0 = 10\,\text{V}$ and frequency $\omega_{dr}/2\pi = 90\,\text{kHz}$). b) Calibration curve for electrodes used to map the applied voltage to the resulting force applied on the nanoparticle.

4
Non-Gaussian state of motion

In this chapter, based on a published paper [63], we present an experimental protocol aimed at achieving state expansion and the emergence of non-Gaussian features in the center-of-mass motion of an optically levitated nanoparticle. The state expansion process leverages a parametric driving scheme involving sudden, non-adiabatic, transitions between two distinct trap frequencies [64]. These frequency switches are implemented using square wave pulses, which temporarily reduce the power of the trapping laser before restoring it to its original value.

The particle's state begins as a thermal state and is characterized by a circular Gaussian distribution in phase space. The effect of the pulses initially manifests as a elongation in the phase space distribution of the system. A sudden reduction in trap stiffness, achieved by a decrease in trapping potential, lowers the system's potential energy while leaving the kinetic energy unchanged. Due to the non-adiabatic nature of the pulse, the state does not instantaneously adapt to the new potential, and the subsequent evolution unfolds over the next quarter of the oscillation period, where the density function evolves in phase space.

Points initially aligned along the position axis, having lost potential energy, rotate toward the momentum axis as their energy converts into kinetic form, resulting in reduced momentum amplitudes. Conversely, points along the momentum axis, retaining their kinetic energy, extend into larger position amplitudes as they evolve in the softened potential. This process transforms the initially circular phase space distribution into an ellipsoidal shape with the semi-major axis aligned along the position axis.

The rising pulse restores the trap stiffness to its original value. In the subsequent quarter-period of oscillation within the stiffer trap, the dynamics project the semi-major axis of the ellipse further along the momentum axis. Simultaneously, the smaller momentum values along the position axis recede even further, refining the ellipsoidal distortion in phase space.

As the next cycle of the square wave begins, the already elongated phase space density undergoes the same transformation, further stretching into an even longer elliptical shape. Repeated application of such pulses progressively increases the oscillation amplitude of the particle, enabling it to explore the non-linear, flatter extremities of the trapping potential (Fig. 2.3) while remaining stably confined. This expansion into the non-linear regime allows the dy-

namics to capture Duffing-like non-linearities, as previously demonstrated [65]. This scheme dynamically shapes the potential landscape creating bi-stability. Classical effects have been discussed before, applied in fields such as memory elements [66], signal amplification via stochastic resonance [67], non-equilibrium physics [68], nonlinear dynamics, synchronization [69], and active escape dynamics [70]. It is also predicted to enhance force sensing capabilities of levitated mechanics [71].

4.1 Theoretical model

We refer to the setting illustrated in (Fig. 4.1A), which depicts a nanoparticle trapped in an optical tweezer in vacuum. In general, the particle motion occurs in all three spatial directions (x, y, z), including cross coupling between orthogonal directions of motion [69] and possibly involving rotational motion as well. However, our analysis is focused only at the x motion.

We model the stochastically driven and damped oscillatory motion of a levitated particle in a vacuum by a one-dimensional Langevin-type equation for the time-dependent position $x(t)$ of the centre-of-mass motion of the particle of mass m in the trap, as discussed in (Sec. 2.5). However, we add a scaling parameter, $S(t)$, to control the scale of the restoring force term of Eq. (4-1) which we control by modulating in time the power of the trapping laser as a mean to implement the frequency pulses as illustrated in (Fig. 4.1B).

$$\ddot{x}(t) = -\Gamma_m \dot{x}(t) + S(t)\frac{F(x)}{m} + \frac{\mathcal{F}_{fluct}(t)}{m}, \tag{4-1}$$

Moreover, the restoring force $F(x)$ in the second term of Eq.(4-1) represents a nonlinear force directed along the gradient of the optical potential. Its form, given by $F(x) = -\partial_x U(x)$, was introduced in Eq.(2-7). The optical trapping potential, $U(x)$, for the parabolic mirror configuration is approximated as $U(x) = \omega^2 x^2 + w^2 \xi x^4$, where $\xi = -0.1\,\mu\mathrm{m}^{-2}$ characterizes the softening Duffing nonlinearity. This parameter was experimentally determined, as detailed in Ref.[65]. To validate the experimental findings, computer simulations, described in (Sec.2.8), were conducted and compared with the collected data.

4.2 Experiment

The experimental setup is illustrated in (Fig. 4.1A). We use a parabolic mirror to focus light at the wavelength of 1550 nm to a diffraction-limited spot of the diameter of 1μm. A pulse generator (Berkeley BNC 525) and an electro-optical modulator (EOM, Jenoptik AM1550b) are used to modulate

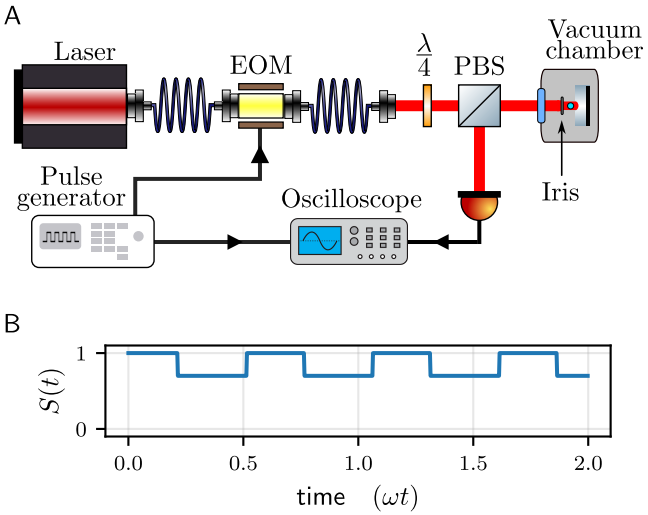

Figure 4.1: **Panel A:** Schematic of experimental setup. A silica nanoparticle is trapped by an optical tweezers in vacuum. An electro-optical modulator (EOM) controlled by a pulse generator modulates the power of the laser. The oscilloscope receives the signal from the particle. Its acquisition is triggered by a synchronous signal from a pulse generator. **Panel B:** Illustration of the square wave signal generated by the pulse generator, used to alternate the trap frequency between two distinct values. The timing of the pulses is designed to allow precisely one quarter of an oscillation period at each power level.

the laser intensity as a square-wave with high and low levels of 80 mW and 57 mW respectively, to trap a silica particle of close to spherical shape (460 nm diameter) from a spray in the focal point. We monitor the centre-of-mass motion of the trapped particle by detecting a small fraction of Rayleigh back-scattered light from the trapping field with a single photodiode detector [72].

4.3 Data analysis

The calibration of motional amplitudes and the mass of the trapped particle was performed under the assumption of perfect thermal equilibrium between the particle and the surrounding gas at 5 mbar and 300 K. This was achieved by fitting a Lorentzian curve to the trap frequency peak, as shown by the green curve in Fig.4.2, following the procedure outlined in Ref.[72]. This approach allows the signal variance, measured in volts, to be directly related to the thermal energy via the equipartition theorem, thereby providing a conversion factor from volts to meters.

Here, we detail the procedure for extracting the x-component of the particle's motion through careful filtering. This process requires precision, as it is well-established that improper filtering can significantly distort a signal.

The time-domain signal from the photodiode encodes information about

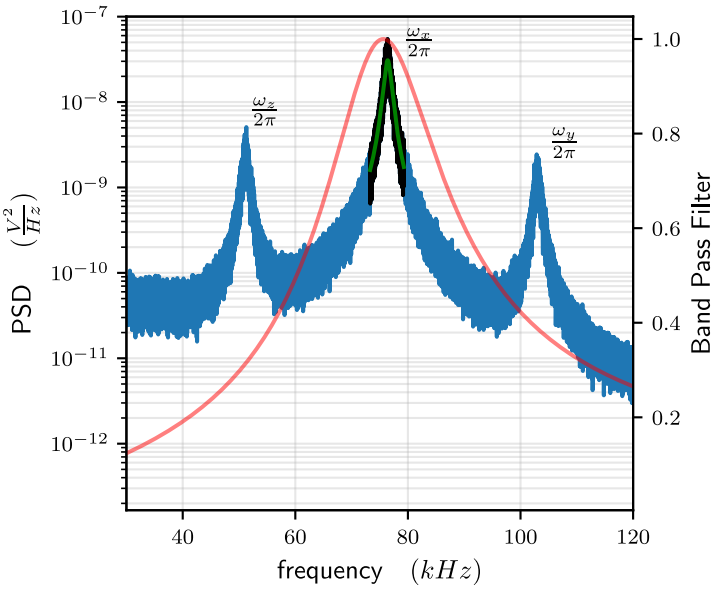

Figure 4.2: PSD signal showing peaks at all three (z, x, y) directions of motion. Green curve represents the curve fit of a Lorentzian at the relevant direction of motion of the experiment. Band-pass filter function, in red, applied to isolate only the x-component of the detected signal for further analysis.

the particle's motion along all three spatial axes (x, y, and z). To analyze these components, the time-domain signal is converted into a power spectral density (PSD) in the frequency domain, following the methodology described in Ref. [72]. The motion along the x, y, and z-axes manifests as distinct peaks in the PSD, corresponding to their respective frequencies.

To isolate the x-component, we apply a discrete band-pass filter in post-processing to the raw signal. The filter function is illustrated in Fig. 4.2. Special care is taken to ensure that the filtered signal accurately represents the x-motion and is not significantly altered by the filtering process. The optimal results are achieved using a first-order band-pass filter with a bandwidth of 2 kHz centered around the frequency $\omega_x/2\pi$, as shown by the red curve in Fig. 4.2. This approach ensures minimal distortion while effectively isolating the desired component.

The effect of an abrupt change of the filter function applied to the time-domain signal can be evaluated by checking the attenuation of a unit impulse response, $U(t - t_0)$ for a pulse applied at time t_0. Unit impulse response is measured on a dB-power scale. The attenuation of the unit impulse response given by $A = 20 \log_{10} |U(t - t_0)|$ is used to evaluate the distortion requirement. Our set target is to achieve attenuation below -80 dB and to minimize the transient time for the impulse to attenuate to this level. For the filter used in the experiment the transient time is 94.53 μs which corresponds to about

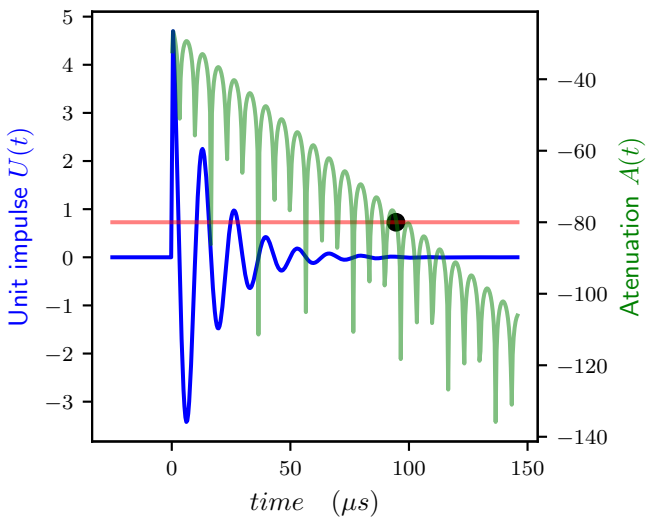

Figure 4.3: Transient time for a impulse to be attenuated by the filter. The blue line is the unit impulse response generated by the rapid change of the filter function. The goal is to identify filter setting which minimise the ring-down time of the unit impulse after applying the filter function. The green line is the corresponding attenuation of the filter and is used to evaluate such decay time. Our benchmark value of -80 dB attenuation is marked as red line. The black dot is a marker when the targeted attenuation has been achieved, which is after seven oscillations of the particle trapped in our experiment.

seven periods of the particle's oscillation and is represented by the black point in Fig. 4.3. This consideration is relevant since the squeezing pulses $S(t)$ can work as a unit impulse and unfavorably affect the processed signal.

To prepare bimodal states of motion the pressure is further reduced to 1×10^{-2} mbar and the particle resonance frequency $\omega/2\pi = 77\,\text{kHz}$ is evaluated from the spectrum of the signal at the high-power level. Next, state expansion is achieved modulating the scale of the restoring force term of Eq. (4-1) as,

$$S(t) = \begin{cases} 1, & \text{for } t' = 0 \text{ or } t' \in [\tau_{low}, \tau_{low} + \tau_{high}], \\ 0.71, & \text{for } t' \in [0, \tau_{low}]. \end{cases} \tag{4-2}$$

Here $t' = t \mod (\tau_{low}+\tau_{high})$. Each pulse is timed so that the particle completes a quarter of an oscillation at the high-power level, $\tau_{high} = \pi/2\omega = 3.25\,\mu$s, and another quarter of an oscillation at the low-power level, $\tau_{low} = \pi/2\omega\sqrt{S} = 3.48\,\mu$s. The duration at the low-power level is slightly longer due to the re-scaling of dynamics by the relative decrease of power as seen by the longer negative pulses of (Fig. 4.1B). The particular value of low power level scaling could not be too small since it would exaggerate the dynamical effects on the particle to the extent that it would get ejected from the trap. Langevin simulations were a valuable tool to find suitable parameter regimes.

One pulse sequence consists of a train of 55 pulses as constructed on the

pulse generator to prepare the bimodal state, seen in green in the top plot of (Fig. 4.4A). Data acquisition by the oscilloscope was synchronised with the pulse generator and 689 pulse sequences are acquired with 518 ms between successive sequences which is about 25 times longer than the extracted 20 ms relaxation time, in good agreement with Eq.(2-12), allowing the particle to relax back to the thermal state between consecutive runs.

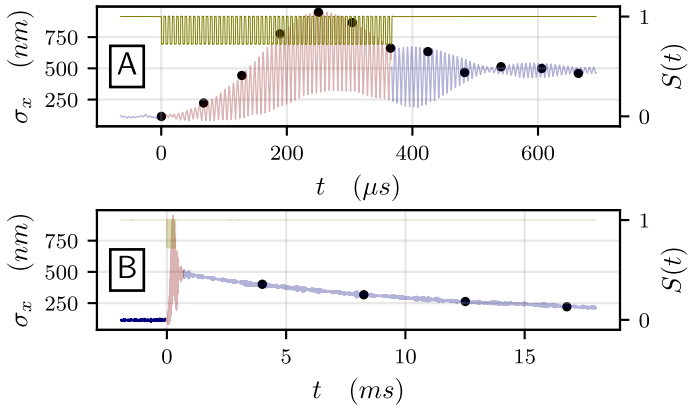

Figure 4.4: Experimental time evolution of the standard deviation of the particle position as measured by the photodiode (Blue/red line). Green line is the intensity modulation function $S(t)$, see (Eq. 4-1), applied to the trapping laser beam via the EOM. *Panel A*: Dynamics at μs time scale showing details of pulses and transient of state formation. *Panel B*: Dynamics at ms scale allowing visualization of thermalisation due to gas collisions.

The particle's velocity is inferred from position time series by numerical differentiation. Each of the 689 experimental run produces a point in the phase space that evolves in time as the pulse sequence is carried out. The time evolution of this ensemble provides statistics for estimating the state density distribution in the phase space, shown in (Fig. 4.5).

4.4 Computer simulation

We have integrated (Eq. 4-1) numerically using the Euler-Maruyama method and sampling the initial values of position and momentum of the particle from a thermal state as described in (Sec. 2.8). The results of our analysis are shown as the phase-space probability distributions in (Fig. 4.6A-C) showing that our one-dimensional description of the dynamics is sufficient to produce the main features of experimental data.

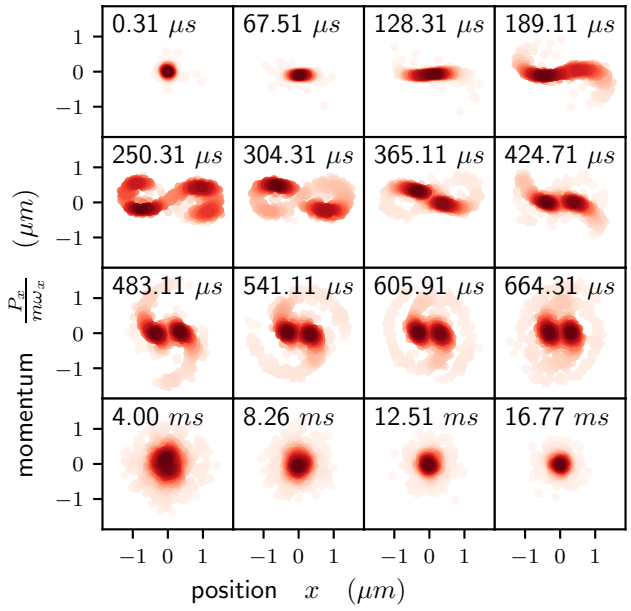

Figure 4.5: Experimental time-trace of the phase-space distribution of an initial thermal state of motion of the particle subjected to our protocol. Snapshots of distribution are indicated as black dots in (Fig. 4.4).

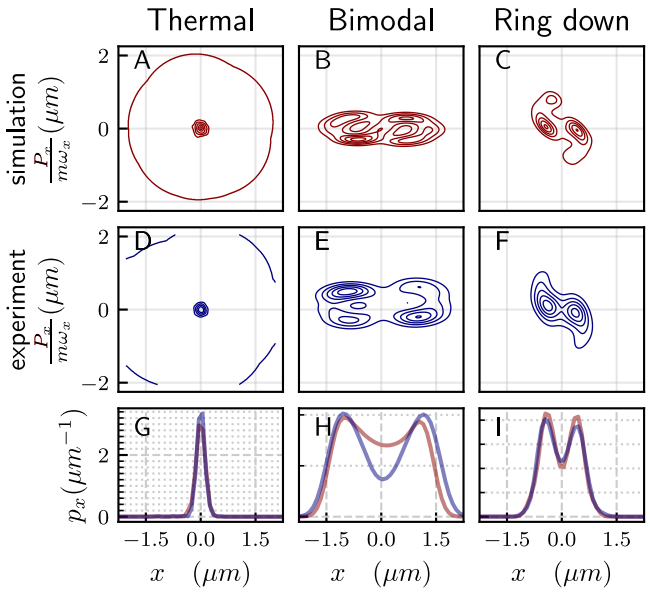

Figure 4.6: Comparisons between simulations (red lines) and experimental reconstructions (blue lines) of the phase-space distributions associated with paradigmatic states of motion of the levitated particle. **Panels A and D:** Initial thermal state; **Panels B and E:** initial non-Gaussian bimodal state; **Panel C and F:** The initial distribution is that of the motional state achieved by stopping the dynamical protocol. Such state will eventually relax back to a thermal configuration. **Panels G, H and I:** projection of the phase-space distribution, with p_x the position probability function for the three initial states described above.

4.4.1 Results and Discussion

The trap non-linearity generating the non-Gaussian state is small in typical experimental conditions [48]. Taylor expansion of the gradient force up to third order shows that the inverse of the Duffing parameter is proportional to the square of the beam's waist. Considering it as a measure for the range of nonlinearity, we note that it is larger than the spread of the thermal state $\sigma_{thermal} = \sqrt{k_B T/k}$, where k is the optomechanical spring constant and T the motional temperature. This means that the particle hardly visits the nonlinear part of the potential. By squashing the motional state, we induce sufficient elongation such that the vertexes of the state are eventually extended to nonlinear parts of the potential well and the non-linear effect dominates the dynamics. In these regions, the particle's dynamics is slower due to a softer effective spring constant making the tip of the ellipse lag behind compared to the faster harmonic behaviour near the centre. In the course of sufficiently many weak pulses, the state changes its shape, steadily transforming it from the initial circular thermal Gaussian to a squashed ellipsoidal and eventually to curved spiral where probability mass starts to accumulate, forming a multi-modal state.

To quantify the non-Gaussianity of the resulting simulated and experimentally obtained states, we adopt a non-dimensional measure of bi-modality [73],

$$A_D = \frac{\sqrt{2}}{\sigma_T}|\mu_1 - \mu_2|, \tag{4-3}$$

where $\mu_{1,2}$ are the positions of the peaks of the distribution and $\sigma_T = \sqrt{\sum_{i=1}^{2} \sigma_i^2}$ is defined in terms of the individual peak's variances $\sigma_{1,2}$ [cf. Fig. 4.6H]. By curve fitting a double Gaussian function to our experimental and simulated data we find the values of $A_D^{exp} = 3.95$ and $A_D^{sim} = 3.32$ in good agreement with 12% deviation which we identify to be originated by a small difference in the shape of the real trapping potential from the simulated one. The influence of the potential's non-linearity is understood to be negligible in the linear section near the trap centre and to become dominating towards the asymptotically flat edges of the optical trap. Despite knowing general features of the non-linearity of the potential well, its exact profile is not experimentally known. As such, simulations assuming an ideal sharp beam profile were found to deviate more from the experimental results. We also find that the experimental thermal state has some outlier points that overextend the tails of Gaussian distribution, which are not included in the simulations and contribute to a softening of the

potential and a larger value for A_D^{exp}. We explain outliers by a build-up of amplitude as a net effect from multiple collisions by background gas particles or other perturbations affecting the trap.

4.5 Pre-cooled state

The quantum regime of this scheme has been shown in an analogous circuit QED architecture [74]. Moreover, theoretical estimations [75] show a quantitative perspective for levitated nanoparticles and the emergence of genuine quantum features of motion from a sufficiently coherent initial state of the particle [25, 24, 26, 27, 76]. In the quantum regime this would result in negative phase-space distributions, thus unambiguously demonstrating non-classicality, reminiscent of Schrödinger cat-like states of significant relevance for quantum information processing and fundamental tests of quantum mechanics.

To bring the experiment closer to the quantum regime, we repeated the same protocol with the addition of feedback cooling to initialize the particle in a state with a lower phonon occupation number [72, 77]. Experimentally, this was achieved using lock-in amplifiers which track the movement of the particle and provide the control signal suitable for cooling it's COM motion, as illustrated in the experimental setup shown in (Fig. 4.7).

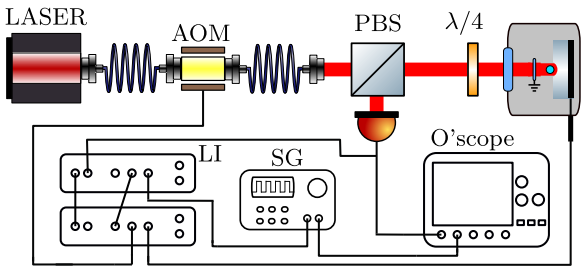

Figure 4.7: **Experimental setup for pulse-driven state expansion:** Schematic of experimental setup. A silica nanoparticle is trapped by an optical tweezers in vacuum. An acusto-optical modulator (AOM) controlled by a signal generator (SG) and lock-in amplifier (LI) modulates the power of the laser, which serves as the mechanism to modulate the intensity of the driving laser and thus control the trapping potential of the particle. The oscilloscope (O'scope), triggered by a synchronous signal from the SG, records the signal from the particle. The polarising beam splitter (PBS) and $\lambda/4$ waveplate routes the particle's movement signal towards a photo-detector. The particle displacement is detected to implement parametric and electric cooling mechanisms to lower the energy of the translational degrees of freedom of the system in three directions (only one direction shown in the figure).

All data analysis procedures followed the same methodology as described in the previous experiment. An example of data from a single experimental run

is shown in (Fig.4.8). The time evolution of the density function is illustrated in (Fig.4.9), while the key experimental parameters are summarized in (Tab. 4.1).

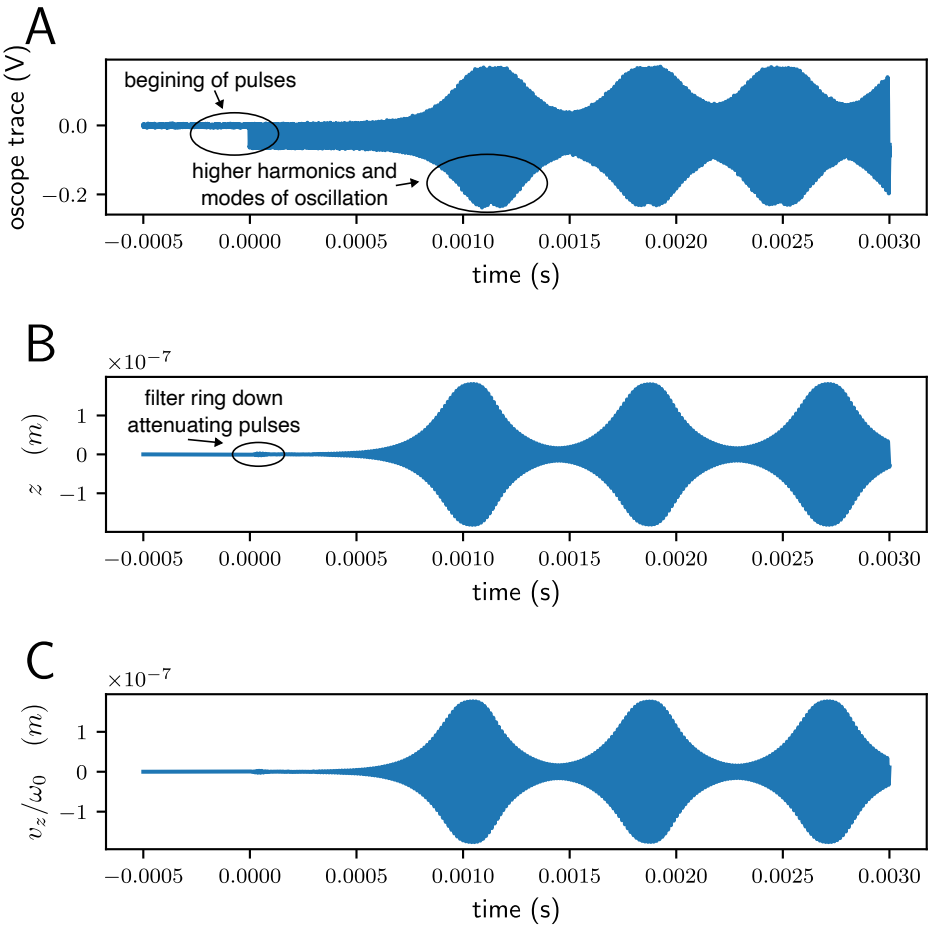

Figure 4.8: **Panel A**: Raw time trace recorded by the oscilloscope in Volts. It is possible to **Panel B**: Filtered time trace converted to SI units. **Panel C**: Numerically differentiated position time trace, used to infer the particle's velocity. The plots **B** and **C** shows the time evolution of a single point in the position-velocity phase space. This process is repeated for all experimental runs and the dense scatter plot shown in Fig. 4.12 is produced

Parameter	Value
$\omega_x/2\pi$	137.0 kHz
$\omega_y/2\pi$	106.4 kHz
$\omega_z/2\pi$	77.6 kHz
pressure	3×10^{-7} mbar
mass	7.54×10^{-18} kg
Cooled state position variance	$(3.21 \pm 0.11) \times 10^{-20}\,\mathrm{m}^2$
Cooled state momentum variance	$(4.12 \pm 0.14) \times 10^{-43}\,\mathrm{kg}^2\mathrm{m}^2\mathrm{s}^{-2}$
Cooled state ocupation number	(1154.3 ± 42.3)

Table 4.1: Summary of experimental parameters.

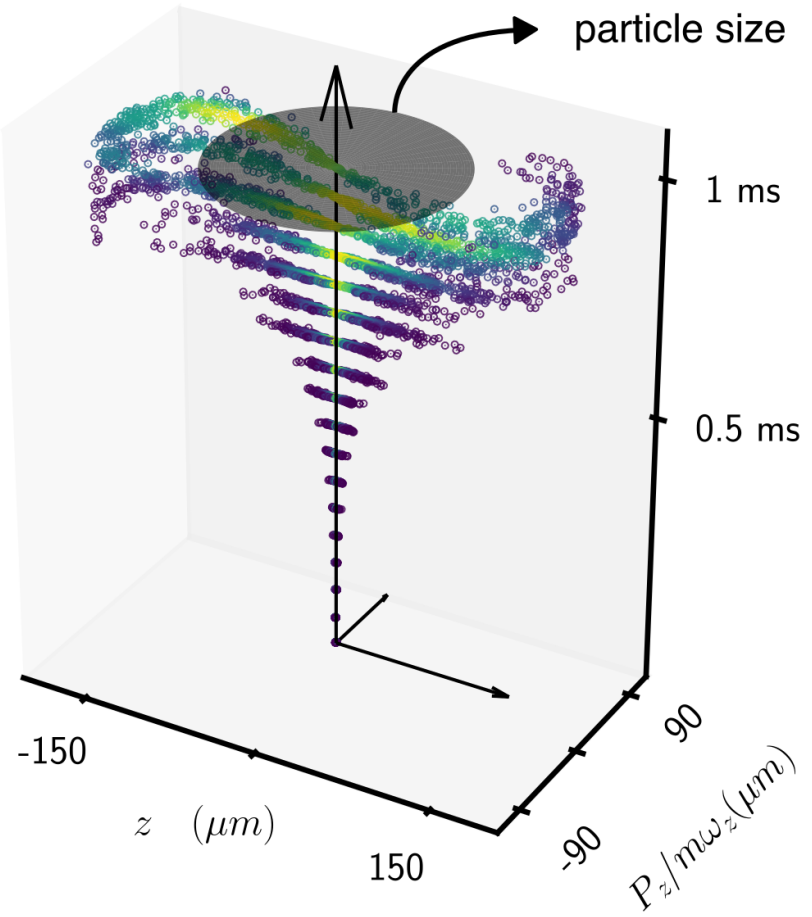

Figure 4.9: Levitated nanoparticle's position-momentum phase space expansion of an initial low ocupation phonon thermal state. The state expands beyond the linear size of the particle itself and eventually develop non-Gaussian features from the nonlinear tails of the optical potential.

By fitting a Lorentzian profile to the spectrum of each harmonic trap frequency and applying the equipartition theorem at an assumed temperature of 300 K, we calibrate the system and subsequently calculate the position variance of the z translational mode as $\sigma^2_{300K} = (2.30 \pm 0.03) \times 10^{-15}\,\mathrm{m}^2$. The detected signal of particle's displacement is used to cool its three translational degrees of freedom, while the pressure is brought down to 3×10^{-7} mbar. The transversal x and y modes are cooled by parametric feedback all the way down to a level ensuring that the translational degrees of freedom are mutually decoupled. We can thus focus on one mode only and treat the problem as quasi-one-dimensional for the z axis. Such mode is cooled electrically by cold damping using an electrode actuating on the charged particle with a uniform electric field proportional to the particle's z velocity. The cooled state has a position variance $\sigma^2_{\mathrm{cold}} = (3.21 \pm 0.11) \times 10^{-20}\,\mathrm{m}^2$, which corresponds to an

effective centre-of-mass temperature of

$$T_{\text{eff}} = 300\,\text{K} \times \frac{\sigma^2_{\text{cold}}}{\sigma^2_{300\text{K}}} = (4.18 \pm 0.15)\text{mK}, \tag{4-4}$$

and mean occupation number $\bar{n} = (e^{\hbar\omega_z/k_B T_{\text{eff}}} - 1)^{-1} = (1154.3 \pm 42.3)$ phonons, k_B standing for Boltzmann's constant. Fig. 4.11 illustrates the growth of the semi major axis, during the initial pulses within the first 1 ms of the protocol. With the system remaining in the harmonic approximation of the potential the expansion is exponential. This rapid expansion stage is driven by the protocol's dynamics and is characterized by a time constant of $\tau_{\text{protocol}} = 68.6\,\mu$s, which is much faster than the thermalization due to gas collisions, occurring on a timescale of seconds at the experimental pressure, as described by (Eq. 2-12).

The initial exponential expansion continues up to $t_{peak} = 1.07$ ms, when we reach the first peak of the curve. At such time, we have an expansion of 28.4 dB, which corresponds to $\sigma_z(t_{peak}) = 124$ nm. Remarkably, this is 24% larger than the nanoparticle dimension, and 158% larger than the corresponding thermal spread at 300 K, which is quantified by the expression [78]

$$\lambda_{th,T} = \sqrt{\frac{\hbar}{2m\omega_z} \coth\left(\frac{\hbar\omega_z}{2k_B T}\right)}. \tag{4-5}$$

After the initial exponential expansion, the non-linearity of the trap kicks in and the expansion starts a damped oscillatory behavior and stabilize in an steady state non-equilibrium configuration, characterized by a non-Gaussian multi-modal distribution as discussed previously.

After 6.7 ms, the protocol stops to leave room for feedback, which causes the non-equilibrium state to relax toward the asymptotic, cold state with an initial exponential time constant of $\tau_{\text{feedback}} = 44$ ms as seen in (Fig. 4.10).

4.6 State tomography

The phase-space distributions discussed so far are classical, inferring velocity from position data, and fail to capture the full quantum behavior of the system. To achieve quantum state tomography and reconstruct the Wigner function, the inverse Radon transform (Eq.4-6) is employed. This method integrates the position probability marginal over projection angles that uniformly evolve during one oscillation period, as outlined in Ref.[39]. Under harmonic oscillator dynamics, the Wigner function undergoes uniform circular motion in phase space, naturally providing access to position probability marginals across a full cycle of projection angles. This is analogous to the rotation of medical tomography scanners but eliminates the need for actively

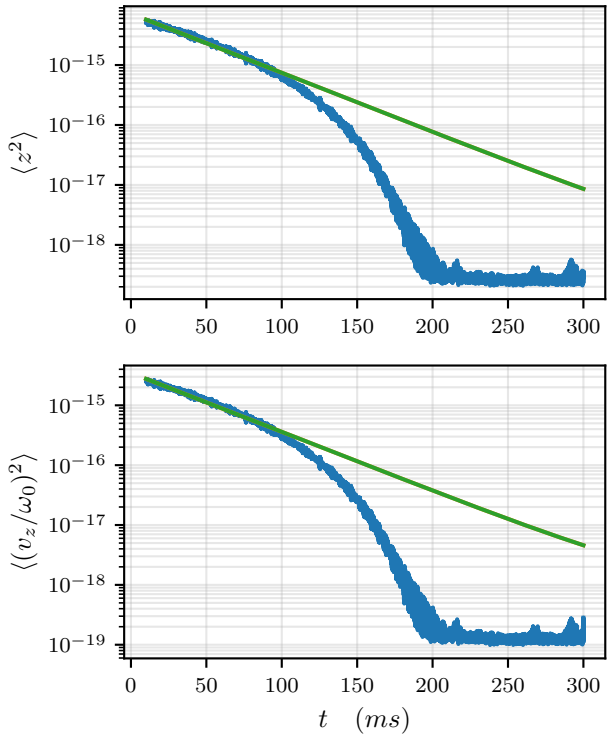

Figure 4.10: **Non-Gaussian to low phonon state:** After the pulse sequence concludes, the particle evolves into a non-Gaussian state. At this point, feedback cooling is applied to drive the particle back into a cooled state.

rotating the projections. Here, the position probability density recorded over a complete cycle serves as projection data, forming the input for the inverse Radon transform to reconstruct the phase-space distribution, as illustrated in Fig. 4.13.

$$W(x,y) = \int_{-\pi}^{\pi} \int_{-\infty}^{\infty} \rho_x(\theta, s)\, \delta(s - x\cos\theta - y\sin\theta)\, ds\, d\theta, \tag{4-6}$$

This method provides a more comprehensive representation of the phase-space distribution by relying solely on position information while enabling the detection of negativity—a defining feature of quantum mechanics that emerges in the presence of quantum coherence. Validation with QuTiP confirms that quantum superposition states can be accurately reconstructed using the inverse Radon transform, provided the state's coherence remains largely intact over a complete oscillation cycle. The method functions analogously to a shutter, requiring at least one full oscillation for reconstruction. Deviations from this requirement, due to decoherence or other factors, result in a blurred and less accurate phase-space representation.

The experimentally detected position trajectory, recorded as a time-resolved dataset by the oscilloscope, captures the particle's oscillatory motion in vectorized form. These trajectories are processed to estimate the time-

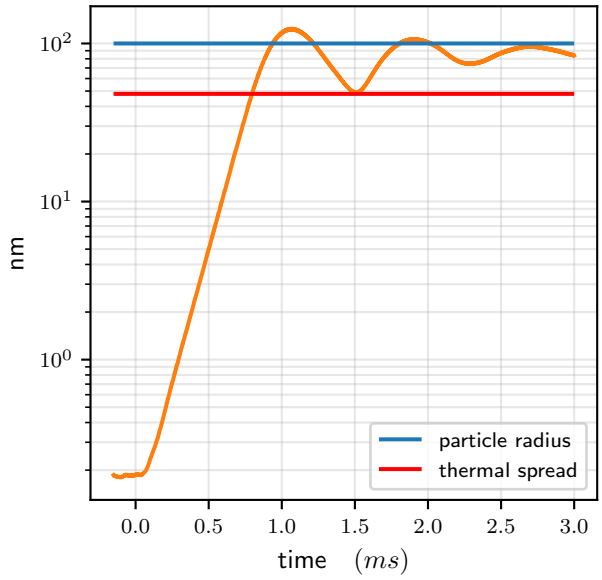

Figure 4.11: **Time evolution of the standard deviation of the instantaneous position quadrature.** For comparison, we report the nanoparticle radius r and the thermal spread $\lambda_{th,300K}$ respectively as a blue and red straight line. Within the first 1 ms, at an exponential timescale of $\tau_{\text{protocol}} = 68.6\,\mu$s, the controlled dynamics of the nanoparticle results in a spatial expansion that exceeds the physical size of the particle itself. After the initial exponential expansion, the non-linearity of the trap kicks in and the expansion starts a damped oscillatory behavior and stabilize in an steady state non-equilibrium configuration, characterized by a non- Gaussian multi-modal distribution

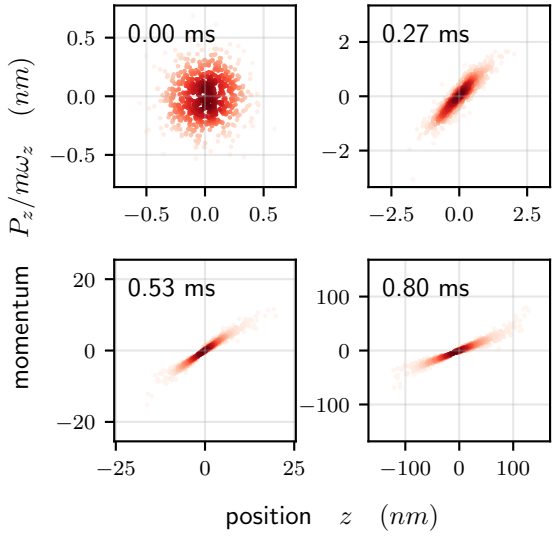

Figure 4.12: Phase-space distribution of position and momentum for the nanoparticle. From top-left subpanel we show the evolution of an isotropic initial state at 4.2 mK within a 0.8 ms timeframe.

dependent position probability density function, which is subsequently represented in a rasterized format known as a sinogram in tomographic imaging.

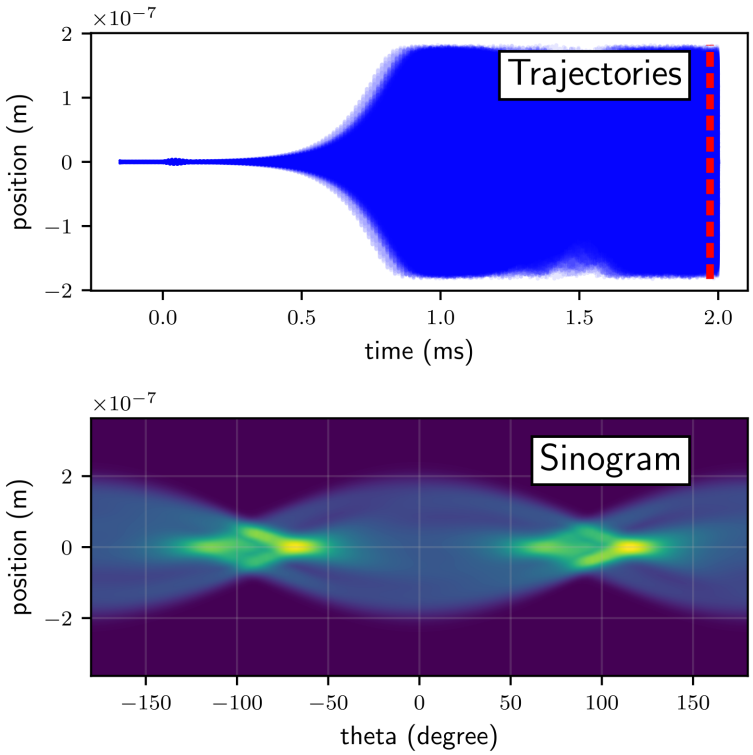

Figure 4.13: **Trajectories:** A plot of multiple trajectories acquired during each experimental run over the initial segment of the expansion protocol. The red lines near 2 ms demarcate a data segment containing one complete oscillation period $(-\pi, \pi)$, which is necessary for the inverse Radon transform. **Sinogram:** The probability density estimate derived from the red-marked segment near 2 ms, represented in a tomographic sinogram format.

A sinogram provides a two-dimensional representation of projection data collected at various angles, serving as the foundational input for reconstructing the phase-space distribution via the inverse Radon transform. In practice, this reconstruction is efficiently implemented using image processing library tools.

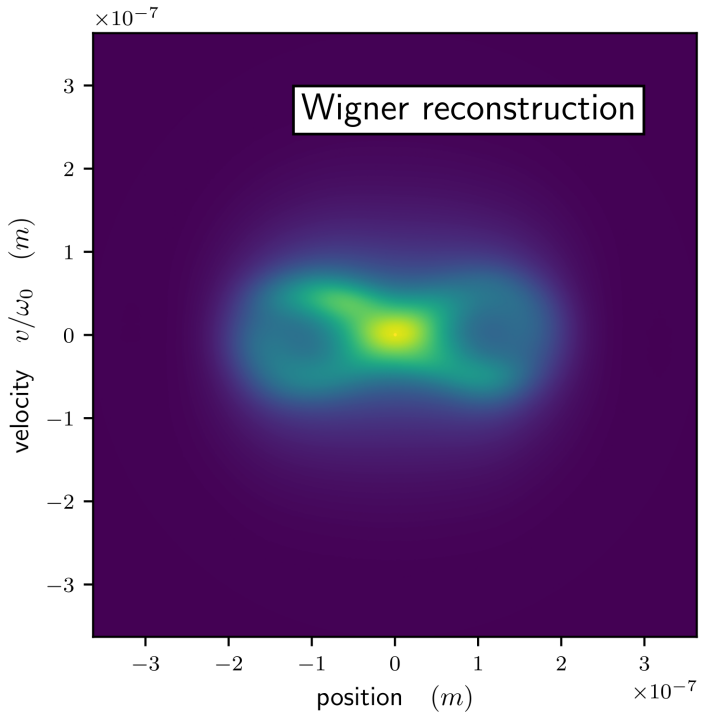

Figure 4.14: Reconstruction of the Wigner function from the sinogram in (Fig. 4.13) using the inverse Radon transform algorithm.

5
Detection model

In this chapter we theoretically examine the scattering information patterns of a dipolar nanoparticle illuminated by arbitrary paraxial structured light fields with uniform polarization. These directional information patterns enable us to predict the probability of detecting a scattered photon that encodes information about the nanoparticle's center-of-mass (COM) position along the orthogonal x, y and z axes, as a function of the spherical coordinates θ, ϕ. Our objective is to compute the total imprecision power spectral density (PSD), integrated over the solid angle. Furthermore, we evaluate the effective detection efficiency for motion along the x, y, z directions.
The discussion on position detection presented here, assumes that the optical field is used solely for detecting the particle's COM position and does not necessarily provide the restoring force. This assumption allows for levitation by alternative means, such as electric or magnetic fields [15]. Additionally, we consider the probe light within the paraxial approximation, enabling the use of Hermite-Gaussian modes.

5.1
Setup

5.2
Dipole Recoil Hamiltonian

We operate under the dipole approximation by considering a nanoparticle with a radius much smaller than the wavelength of the probe beam, effectively treating it as a point-like dipole. In this regime, the nanoparticle's scattering properties are governed by its polarizability α, which encapsulates the response of the material to the incident electric field. The incident electric field of the probe induces a dipole moment $\mathbf{p}$ in the nanoparticle, described by $\mathbf{p} = \alpha\mathbf{E}(\mathbf{r})$, where $\mathbf{E}(\mathbf{r})$ is the local electric field at the nanoparticle's COM position $\mathbf{r}$.

The interaction between the induced dipole and the oscillating electric field results in a potential energy given by $\mathcal{E} = \frac{\alpha}{2}|\mathbf{E}(\mathbf{r})|^2$. This energy represents the cost of polarizing the nanoparticle in response to the external field and will give rise to the interaction Hamiltonian between light field and mechanical modes.

In our setup, the total electric field at the position of the nanoparticle has two contributions: the classical probe field $\mathbf{E}_{pr}(\mathbf{r}, t)$ and the quantized free electromagnetic field $\hat{\mathbf{E}}_f(\mathbf{r})$. Thus, the combined electric field is given

by $\hat{\mathbf{E}}(\mathbf{r},t) = \mathbf{E}_{pr}(\mathbf{r},t) + \hat{\mathbf{E}}_f(\mathbf{r})$. We assume that the probe field dominates, such that $|\langle\hat{\mathbf{E}}_f(\mathbf{r})\rangle| \ll |\mathbf{E}_{pr}(\mathbf{r},t)|$, for any relevant states of the free field. This allows us to simplify the interaction Hamiltonian by neglecting terms of order $\mathcal{O}(|\langle\hat{\mathbf{E}}_f(\mathbf{r})\rangle|^2)$.

This approximation is key for our analysis, as it reduces the complexity of the system and allows us to primarily consider the effect of the structured probe light on the nanoparticle's position detection, while the influence of the vacuum fluctuations from the free electromagnetic field remains a small perturbation.

$$H_I = -\frac{1}{2}\alpha\mathbf{E}_{pr}(\mathbf{r},t)^2 - \alpha\mathbf{E}_{pr}(\mathbf{r},t)\cdot\hat{\mathbf{E}}_f(\mathbf{r}), \tag{5-1}$$

The first term in the interaction Hamiltonian represents the optical potential, which generates the restoring force necessary for trapping and stabilizing the particle through optical levitation. This term describes the conservative interaction between the induced dipole moment of the nanoparticle and the oscillating electric field of the laser, effectively creating a potential well that confines the particle.

However, in our analysis, we will neglect this term, assuming that the particle is trapped by an external mechanism (e.g., electrostatic or magnetic fields) rather than relying on the optical potential for confinement. Instead, our focus will be on the second term in Eq. (5-1), which describes the dipole recoil Hamiltonian.

The dipole recoil Hamiltonian captures the interaction between the induced dipole moment of the nanoparticle and the scattered photons, leading to recoil effects. These recoil kicks result in momentum transfer that influences the particle's mechanical motion, contributing to heating and momentum diffusion.

This same Hamiltonian also describes how the particle's motion modulates the scattered light, coupling the center-of-mass position to changes in the electromagnetic field. As a result, variations in the scattered light carry information about the nanoparticle's movement.

Thus, the dipole recoil Hamiltonian plays a dual role: it governs the recoil effects influencing the mechanical dynamics and provides the fundamental mechanism for optically detecting the particle's motion through the scattered light field.

$$H_{recoil} = -\alpha_p\mathbf{E}_{pr}(\mathbf{r},t)\cdot\hat{\mathbf{E}}_f(\mathbf{r}). \tag{5-2}$$

5.2.1 Probe Electric field

Lets consider illumination by a paraxial structured light beam with uniform polarization along x axis, $\mathbf{u_x}$. The beam is generated by a coherent superposition of Hermite-Gaussian (HG) modes, where the complex coefficients $c_{mn} = a_{mn} + ib_{mn}$ determine the relative weights and phases of each mode. The phase of the beam consists of three components: the Gouy phase shift $\psi_{mn}(z) = (m + n + 1)\arctan(z/z_r)$, plane wave propagation $k_0 z$ and time evolution $\omega_0 t$. The electric field of the probe beam can be expressed as:

$$\mathbf{E}_{pr}(\mathbf{r}, t) = Re\Bigg\{ \Bigg(\sum_{mn} c_{mn} A_{mn}(\mathbf{r}) e^{i\psi_{mn}(z)}\Bigg) \times e^{-ik_0 z} e^{i\omega_0 t} \Bigg\} \hat{\mathbf{u}}_\mathbf{x}. \tag{5-3}$$

The amplitude, $A_{mn}(\mathbf{r})$, given below, is defined in terms of Hermite polynomials $H_m(x)$ and $H_n(y)$, combined with a Gaussian envelope. It includes a normalization factor $N_{mn} = \frac{1}{w(z)}\sqrt{\frac{2^{-(n+m-1)}}{\pi m! n!}}$, where $w(z)$ is the beam waist. This normalization ensure equivalent power for any mode with arbitrary values of m and n.

$$A_{mn}(\mathbf{r}) = N_{mn} H_m\Big(\frac{\sqrt{2}x}{w(z)}\Big) H_n\Big(\frac{\sqrt{2}y}{w(z)}\Big) \exp\Bigg(-\frac{x^2 + y^2}{w(z)^2}\Bigg). \tag{5-4}$$

In what follows we expand the probe beam field Eq. (5-3) around particle's equilibrium position ($\mathbf{r}$=0) to first order in the position $\mathbf{r}$. To streamline the presentation and avoid cumbersome equations, we introduce the symbols E^P_{pr} and E^Q_{pr} to represent the terms proportional to the cosine and sine components of the time evolution, respectively,

$$\mathbf{E}^{mn}_{pr}(\mathbf{r}, t) \approx \Big[E^P_{pr} \cos\omega_0 t + E^Q_{pr} \sin\omega_0 t\Big] \hat{\mathbf{u}}_\mathbf{x} \tag{5-5}$$

At the origin, the field amplitude is a constant scalar number $A_{mn}(0) = A^{(0)}_{mn}$ and the gradient of the field is a constant vector $\nabla A_{mn}|_{\mathbf{r}=0} = \nabla A^{(0)}_{mn}$. We also define a vector $\mathbf{s}_{mn} = (0, 0, k_0 - \psi'_{mn}(0))^T$ that reflects the effective longitudinal wavenumber close to the focus due to the Gouy phase shift. With these definitions the components of (Eq.5-5) are written as,

$$\begin{aligned} E^P_{pr} =& a_{mn}(A^{(0)}_{mn} + \mathbf{r}\cdot\nabla A^{(0)}_{mn}) \\ &+ b_{mn}A^{(0)}_{mn}\mathbf{r}\cdot\mathbf{s}_{mn}, \end{aligned} \tag{5-6}$$

$$\begin{aligned} E^Q_{pr} =& a_{mn}A^{(0)}_{mn}\mathbf{r}\cdot\mathbf{s}_{mn} \\ &- b_{mn}(A^{(0)}_{mn} + \mathbf{r}\cdot\nabla A^{(0)}_{mn}). \end{aligned} \tag{5-7}$$

5.2.2 Quantized free space field

The free electromagnetic field is treated quantum mechanically with creation and annihilation operators satisfying $[a_\epsilon(\mathbf{k}), a^\dagger_{\epsilon'}(\mathbf{k}')] = \delta_{\epsilon\epsilon'}\delta(\mathbf{k}-\mathbf{k}')$. Where $\mathbf{u}_\epsilon(\mathbf{k})$ is the polarization vector for any mode with wavevector $\mathbf{k}$ and dispersion relation $\omega = c|\mathbf{k}|$. We decompose it into a basis of plane waves as follows

$$\begin{aligned} \mathbf{E}_f(\mathbf{r}) = i\sum_\epsilon \int d^3\mathbf{k}\sqrt{\frac{\hbar\omega}{16\pi^3\varepsilon_0}}\mathbf{u}_\epsilon(\mathbf{k}) \\ \times\left(a_\epsilon(\mathbf{k})e^{i\mathbf{k}\cdot\mathbf{r}} - a^\dagger_\epsilon(\mathbf{k})e^{-i\mathbf{k}\cdot\mathbf{r}}\right) \end{aligned} \tag{5-8}$$

Expanding the free field to first order in the particle's position around $\mathbf{r} = 0$,

$$\begin{aligned} \mathbf{E}_f(\mathbf{r}) \approx \sum_\epsilon \int d^3\mathbf{k}\sqrt{\frac{\hbar\omega}{16\pi^3\varepsilon_0}}\mathbf{u}_\epsilon(\mathbf{k}) \\ \times\left[i\left(a_\epsilon(\mathbf{k}) - a^\dagger_\epsilon(\mathbf{k})\right) - \mathbf{k}\cdot\mathbf{r}\left(a_\epsilon(\mathbf{k}) + a^\dagger_\epsilon(\mathbf{k})\right)\right]. \end{aligned} \tag{5-9}$$

5.3 Coupling constant

With the linearized forms of the probe and free space fields, we can now focus on the dipole recoil Hamiltonian (Eq. 5-2),

$$H_{recoil} = \sum_{mn}\sum_\epsilon \int d^3\mathbf{k}G(\mathbf{k},\epsilon)\times\left\{H^P_{mn}\cos(\omega_0 t) + H^Q_{mn}\sin(\omega_0 t)\right\}, \tag{5-10}$$

where the coupling strength between the probe field and each plane wave mode is expressed by,

$$G(\mathbf{k},\epsilon) = \alpha\sqrt{\frac{\hbar\omega}{16\pi^3\varepsilon_0}}(\mathbf{u}_x \cdot \mathbf{u}_\epsilon(\mathbf{k})). \tag{5-11}$$

The function $G(\mathbf{k},\epsilon)$ quantifies the interaction based on the wavevector $\mathbf{k}$ and polarization ϵ, capturing the overlap between the polarization of the probe field and the scattered field mode. The terms proportional to cosine and sine in (Eq. 5-10) are,

$$\begin{aligned} H^P_{mn} =& i\left(a_\epsilon(\mathbf{k}) - a^\dagger_\epsilon(\mathbf{k})\right) b_{mn}\mathbf{A}^{mn}_0 && (5\text{-}12)\\ &+ \mathbf{r}\cdot\Big[-\mathbf{k}\left(a_\epsilon(\mathbf{k}) + a^\dagger_\epsilon(\mathbf{k})\right) b_{mn}\mathbf{A}^{mn}_0 && (5\text{-}13)\\ &+ i\left(a_\epsilon(\mathbf{k}) - a^\dagger_\epsilon(\mathbf{k})\right)(\nabla\mathbf{A}^{mn} b_{mn} + \mathbf{s}^{mn}\mathbf{A}^{mn}_0\tilde{b}_{mn})\Big] + \mathcal{O}(r^2), && (5\text{-}14) \end{aligned}$$

and

$$\begin{aligned} H^Q_{mn} =& - i\left(a_\epsilon(\mathbf{k}) - a^\dagger_\epsilon(\mathbf{k})\right)\tilde{b}_{mn}\mathbf{A}^{mn}_0 && (5\text{-}15)\\ &+ \mathbf{r}\cdot\Big[\mathbf{k}\left(a_\epsilon(\mathbf{k}) + a^\dagger_\epsilon(\mathbf{k})\right)\tilde{b}_{mn}\mathbf{A}^{mn}_0 && (5\text{-}16)\\ &+ i\left(a_\epsilon(\mathbf{k}) - a^\dagger_\epsilon(\mathbf{k})\right)(-\nabla\mathbf{A}^{mn}\tilde{b}_{mn} + \mathbf{s}^{mn}\mathbf{A}^{mn}_0 b_{mn})\Big] + \mathcal{O}(r^2), && (5\text{-}17) \end{aligned}$$

respectively.

The dipole recoil Hamiltonian (Eq. 5-10) has two main contributions, one oscillating with $\cos(\omega_0 t)$ and another with $\sin(\omega_0 t)$. The term with $\cos(\omega_0 t)$ is represented by

$$\begin{aligned} H^P_{mn} =& \, i\left(a_\epsilon(\mathbf{k}) - a^\dagger_\epsilon(\mathbf{k})\right) a_{mn}A^{(0)}_{mn}\\ &+ \mathbf{r}\cdot\Big[-\mathbf{k}\left(a_\epsilon(\mathbf{k}) + a^\dagger_\epsilon(\mathbf{k})\right) a_{mn}A^{(0)}_{mn}\\ &+ i\left(a_\epsilon(\mathbf{k}) - a^\dagger_\epsilon(\mathbf{k})\right)\left(\nabla A^{(0)}_{mn}a_{mn} + \mathbf{s}^{mn}A^{(0)}_{mn}b_{mn}\right)\Big]\\ &+ \mathcal{O}(\mathbf{r}^2). \end{aligned} \tag{5-18}$$

and the term evolving with $\sin(\omega_0 t)$

$$
\begin{aligned}
H^{Q}_{mn} = & -i\left(a_\epsilon(\mathbf{k}) - a^\dagger_\epsilon(\mathbf{k})\right) b_{mn} A^{(0)}_{mn} \\
& + \mathbf{r}\cdot\Big[\mathbf{k}\left(a_\epsilon(\mathbf{k}) + a^\dagger_\epsilon(\mathbf{k})\right) b_{mn} A^{(0)}_{mn} \\
& \quad + i\left(a_\epsilon(\mathbf{k}) - a^\dagger_\epsilon(\mathbf{k})\right)\left(-\nabla A^{(0)}_{mn} b_{mn} + \mathbf{s}^{mn} A^{(0)}_{mn} a_{mn}\right)\Big] \\
& + \mathcal{O}(\mathbf{r}^2). \qquad (5\text{-}19)
\end{aligned}
$$

Let us now remove the time dependence of the recoil Hamiltonian by applying a rotating wave approximation. This amounts to making the substitution

$$a_\epsilon(\mathbf{k}) \to a_\epsilon(\mathbf{k}) e^{-i\omega_0 t} \qquad (5\text{-}20)$$

and its complex conjugate, and neglecting fast rotating terms at frequency $\pm 2\omega_0$. We get the dipole recoil hamiltonian in the form,

$$
\begin{aligned}
H_p = \sum_\epsilon \int d^3\mathbf{k} \frac{G(\mathbf{k},\epsilon)}{2} \Big\{ & a_\epsilon(\mathbf{k}) \Big[i c_{mn} (A^{(0)}_{mn} + \mathbf{r}\cdot\nabla A^{(0)}_{mn}) \qquad (5\text{-}21) \\
& + c_{mn} A^{(0)}_{mn} \mathbf{r}\cdot(\mathbf{s}_{mn} - \mathbf{k}) \Big] \Big\} + h.c. \qquad (5\text{-}22)
\end{aligned}
$$

.

5.3.1 Interacting modes

In this section, we introduce the interacting modes that simplify the recoil Hamiltonians into the linearized optomechanical interaction (Eq. 5-29). We start with defining the first family of auxiliary modes in the form of a linear combination of the annihilation operators $a_i \propto \sum_\epsilon \int d^3\mathbf{k}\; G_i(\mathbf{k},\epsilon) a_\epsilon(\mathbf{k})$. These correspond to dipole patterns for dipoles oriented along x, y and z.

$$a_i(\omega) \;=\; -\sqrt{\frac{3c}{8\pi\omega^2}} \sum_\epsilon \int d^3\mathbf{k}\; \delta\left(k - \frac{\omega}{c}\right) (\mathbf{u}_i \cdot \mathbf{u}_\epsilon(\mathbf{k}))\, a_\epsilon(\mathbf{k}) \qquad (5\text{-}23)$$

Using $[a_\epsilon(\mathbf{k}), a^\dagger_{\epsilon'}(\mathbf{k}')] = \delta_{\epsilon\epsilon'}\delta(\mathbf{k}-\mathbf{k}')$ and $\mathbf{k}/k = (\sin\theta\cos\phi, \sin\theta\sin\phi, \cos\theta)^T$, we can show that the modes are independent.

$$\begin{aligned}
[a_i(\omega), a^\dagger_{i'}(\omega')] &= \frac{3c}{8\pi\omega^2}\sum_\epsilon \int k^2 dk \int d\Omega \;\; \delta\left(k-\frac{\omega}{c}\right)\delta\left(k-\frac{\omega'}{c}\right)(\mathbf{u}_i\cdot\mathbf{u}_\epsilon(\mathbf{k}))\,(\mathbf{u}_{i'}\cdot\mathbf{u}_\epsilon(\mathbf{k})) \\
&= \frac{3}{8\pi}\delta(\omega'-\omega)\int d\Omega \;\sum_\epsilon (\mathbf{u}_i\cdot\mathbf{u}_\epsilon(\mathbf{k}))\,(\mathbf{u}_{i'}\cdot\mathbf{u}_\epsilon(\mathbf{k})) \\
&= \frac{3}{8\pi}\delta(\omega'-\omega)\,\delta_{ii'}\int d\Omega\;\left(1-\frac{k_i^2}{k^2}\right) = \delta(\omega'-\omega)\,\delta_{ii'}. \qquad (5\text{-}24)
\end{aligned}$$

We also benefit by defining the second family of auxiliary modes in the form $a_{ij} \propto \sum_\epsilon \int d^3\mathbf{k}\; k_j\; G_i(\mathbf{k},\epsilon)$.

$$\begin{aligned}
a_{ij}(\omega) = &-\sqrt{\frac{15c}{8\pi\omega^2 m_{ij}}} \\
&\sum_\epsilon \int d^3\mathbf{k}\;\frac{k_j}{k}\;\delta\left(k-\frac{\omega}{c}\right)(\mathbf{u}_i\cdot\mathbf{u}_\epsilon(\mathbf{k}))\,a_\epsilon(\mathbf{k}). \qquad (5\text{-}25)
\end{aligned}$$

The constant terms are introduced so that the interacting modes also satisfy the commutation relations $[a_{ij}(\omega), a^\dagger_{i'j'}(\omega')] = \delta(\omega'-\omega)\,\delta_{ii'}\delta_{jj'}$. And $m_{ij} = 2-\delta_{ij}$ is a factor that comes out of angular integrals.

The COM degree of freedom is coupled to each mode, with the coupling strength depending on both the propagation direction of the plane wave and its frequency. Using these modes we can rewrite the dipole hamiltonian as,

$$\begin{aligned}
H_p = \int d\omega\; g_p\Big\{&\Big[ic_{mn}A^{(0)}_{mn} \\
&+\mathbf{r}\cdot c_{mn}(i\nabla A^{(0)}_{mn} + A^{(0)}_{mn}\mathbf{s}^{mn})\Big]a_x(\omega) \\
&- c_{mn}A^{(0)}_{mn}k\sum_i\sqrt{\frac{m_{xi}}{5}}r_i a_{xi}(\omega)\Big\}. \qquad (5\text{-}26)
\end{aligned}$$

The interaction modes can be redefined by incorporating certain parameters into the auxiliary modes,

$$\begin{aligned}
b_0(\omega) &= ic_{mn}A^{(0)}_{mn}a_x(\omega), \qquad (5\text{-}27)\\
b_i(\omega) &= c_{mn}(i\partial_i A^{(0)}_{mn} + A^{(0)}_{mn}s^{mn}_i)a_x(\omega) \\
&\quad - c_{mn}A^{(0)}_{mn}k\sqrt{\frac{m_{xi}}{5}}a_{xi}(\omega). \qquad (5\text{-}28)
\end{aligned}$$

Using these modes we can finally rewrite the dipole Hamiltonian in the form of the linearized optomechanical interaction,

$$H_{recoil} = \int d\omega g_p(b_0(\omega) + \sum r_i b_i(\omega)) + h.c. \tag{5-29}$$

where

$$g_p \;=\; \alpha_p \sqrt{\frac{\hbar\omega^3}{24\pi^2\varepsilon_0 c^3}} \;. \tag{5-30}$$

The interpretation of the modes $b_i(\omega)$ is that each of these operators define a spatial mode of the field that carries away information of each coordinate x, y and z of the particle.

5.4 Information pattern

Let us consider a scenario in which a photon from the probe laser interacts with a particle displaced along the i-th position variable and subsequently scatters into the free field. This process can be equivalently described as the i-th interaction mode creating a photon, $b_i^\dagger |0\rangle$. This photon encodes information about the particle's displacement, making its detection of fundamental interest.

Rather than restricting our analysis to a single frequency, ω, we generalize the description by introducing a multi-mode operator weighted by a function $f(\omega)$. This weight function is normalized such that $\int d\omega |f(\omega)|^2 = 1$ and can be chosen to be arbitrarily narrow or broad around a frequency of interest. The corresponding operator is given by,

$$b_i = \int d\omega \, f(\omega) b_i(\omega), \tag{5-31}$$

where $b_i(\omega)$ is defined by (Eq. 5-27).

To proceed, we consider the state $|\psi\rangle = b_i^\dagger |0\rangle$, representing a single photon distributed over the chosen frequency band defined by $f(\omega)$. Our goal is to study the probability of this photon being scattered into a specific direction. To achieve this, we evaluate the free-space number operator acting on the state $|\psi\rangle$,

$$\rho_i(\theta, \phi) = \langle\psi| \sum_\epsilon \int dk k^2 a_\epsilon^\dagger(\mathbf{k}) a_\epsilon(\mathbf{k}) |\psi\rangle \tag{5-32}$$

$$\rho_i(\theta, \phi) = \sum_\epsilon \int dk k^2 \langle 0| b_i a_\epsilon^\dagger(\mathbf{k}) a_\epsilon(\mathbf{k}) b_i^\dagger |0\rangle \,. \tag{5-33}$$

This approach allows us to extract the directional scattering information encoded in the photon's state, as demonstrated with examples in the next sections. To achieve this, we need to evaluate the commutator that appears in the eigen-equation $a_\epsilon(\mathbf{k}) b_i^\dagger |0\rangle = \Big([a_\epsilon(\mathbf{k}), b_i^\dagger] + b_i^\dagger a_\epsilon(\mathbf{k})\Big) |0\rangle$.

$$[a_\epsilon(\mathbf{k}), b_0^\dagger] = ic_{mn} A_{mn}^{(0)} F_x(\mathbf{k}, \epsilon) \tag{5-34}$$

$$[a_\epsilon(\mathbf{k}), b_i^\dagger] = c_{mn}\Big[(A_{mn}^{(0)} s_i^{mn} + i\partial_i A_{mn}^{(0)}) F_x(\mathbf{k}, \epsilon) - A_{mn}^{(0)} k \sqrt{\frac{m_{xi}}{5}} F_{xi}(\mathbf{k}, \epsilon)\Big]. \tag{5-35}$$

In which we defined

$$F_i(\epsilon, \mathbf{k}) = [a_\epsilon(\mathbf{k}), a_i^\dagger] = -\sqrt{\frac{3c}{8\pi k^2}} f(ck)\,(\mathbf{u}_i \cdot \mathbf{u}_\epsilon(\mathbf{k})) \tag{5-36}$$

$$F_{ij}(\epsilon, \mathbf{k}) = [a_\epsilon(\mathbf{k}), a_{ij}^\dagger] = -\sqrt{\frac{15c}{8\pi k^2 m_{ij}}} \frac{k_j}{k} f(ck)\,(\mathbf{u}_i \cdot \mathbf{u}_\epsilon(\mathbf{k}))\,.$$

The scattering modes providing information about the particle dispacement we can compute the dipole information pattern

$$\rho_0(\theta, \phi) \propto \frac{3c}{8\pi k^2}\left(1 - \frac{k_x^2}{k^2}\right)\left|\sum_{m,n}[ic_{mn}\mathbf{A}_0^{mn}]\right|^2 \tag{5-37}$$

$$\rho_i(\theta, \phi) \propto \frac{3c}{8\pi k^2}\left(1 - \frac{k_x^2}{k^2}\right)\left|\sum_{m,n}[ic_{mn}\partial_i \mathbf{A}^{mn} - c_{mn}\mathbf{A}_0^{mn}(k_i - s_i^{mn})]\right|^2. \tag{5-38}$$

5.4.1 The Gaussian beam

The Gaussian beam represents the simplest case of particle illumination, and its scattering modes are illustrated in (Fig. 5.1). There is a scattering contribution independent of the particle's position, as described by (Eq. 5-37), with an angular distribution characteristic of dipole scattering. However, for displacements along the x, y, and z directions, the scattering modes exhibit angular dependence, as outlined in Eq. 5-38. These effects are consistent with classical calculations presented in [79].

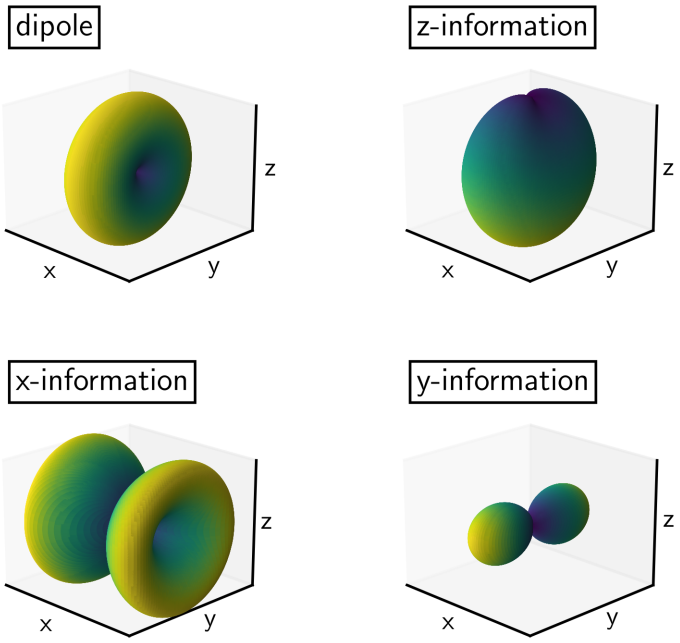

Figure 5.1: **Illumination by the Gaussian beam** Dipole scattering is always present and remains independent of the particle's displacement. In contrast, information about displacements along the x, y, and z directions exhibits a more complex angular dependence. The scattering intensity is represented by both the radial distance from the origin and the color scheme, where yellow denotes high intensity and blue indicates low intensity. However, the color scheme and scale are not consistent across all panels, as the primary goal of the plot is to highlight the directionality of the scattering rather than provide direct intensity comparisons between panels.

The scattering pattern associated with z-displacement (Fig. 5.1) suggests that collecting back-scattered light provides higher information content about the particle's axial displacement. Since the particle's position is encoded in the phase of the scattered field, this indicates that back-scattered light exhibits greater phase sensitivity to z-displacements. Consequently, low oscillation amplitudes are better resolved against the noise floor. However, at high oscillation amplitudes, phase wrapping can occur, leading to distorted signals.

In contrast, front-scattered light exhibits the opposite behavior, making it potentially more suitable for expansion schemes where the particle undergoes large oscillation amplitudes. This behavious is illustrated in (Fig. 5.2).

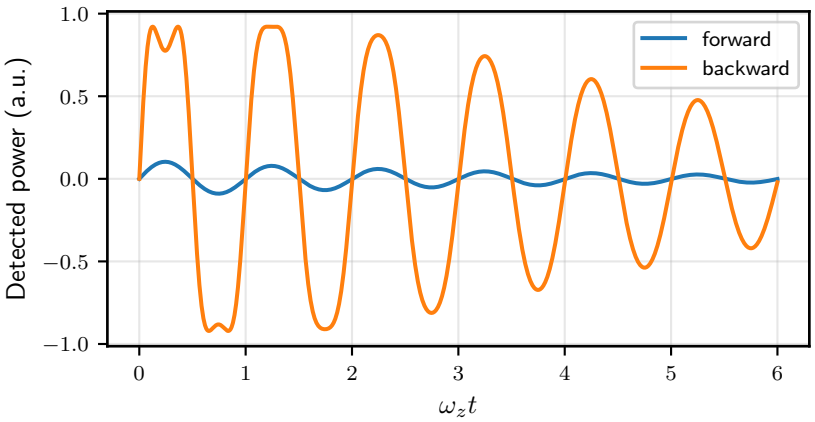

Figure 5.2: **Simulated ring-down dynamics and particle signal detection.** *Backward signal:* Higher phase sensitivity enables better resolution of small motion amplitudes but can result in phase wrapping at large motion amplitudes. *Forward signal:* Exhibits lower phase sensitivity and is more prone to domination by technical noise at low motion amplitudes, as typically observed in ground-state cooling scenarios. However is arguably better for schemes using expanded states with high oscillation amplitudes.

5.4.2 Higher order beams

The HG_{01} mode, depicted in (Fig.5.3A), provides information exclusively about the particle's x-position, as illustrated in Fig.5.3D. This arises because the only non-zero contribution to (Eq. 5-38) is the directional derivative of the field along x. In contrast, the field itself, as well as its derivatives along y and z, vanish.

The HG_{10} mode functions similarly, providing information about the particle's y-position. The resulting scattering pattern is identical to that shown in Fig. 5.3D, with the roles of x and y interchanged.

The $LG_{l=1,p=0}$ mode, shown in (Fig.5.3C), is a linear combination of $HG_{10}/\sqrt{2}$ and $iHG_{01}/\sqrt{2}$. Consequently, it provides position information about both x and y, as illustrated in (Fig.5.3D).

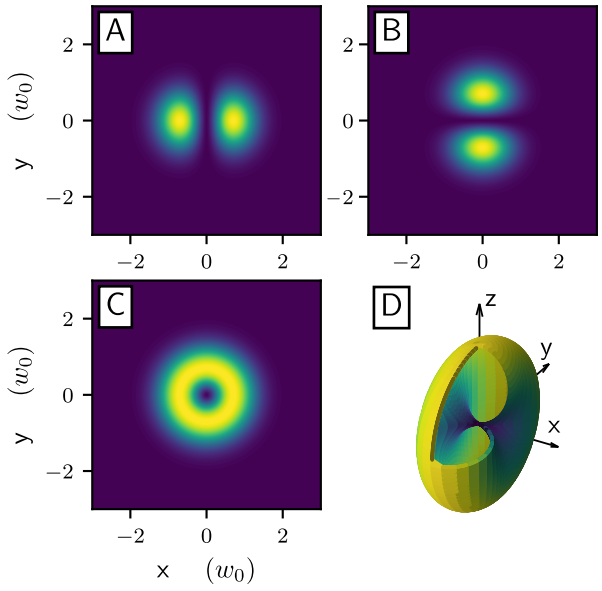

Figure 5.3: **Scattering patterns and position information for Hermite-Gaussian and Laguerre-Gaussian modes.** *(A)* The HG_{01} mode provides information exclusively about the particle's x-position, as only the directional derivative along x is non-zero. *(B)* The HG_{10} mode provides information about the particle's y-position, with a scattering pattern identical to HG_{01}, but with the roles of x and y interchanged. *(C)* The $LG_{l=1,p=0}$ mode is a linear combination of $HG_{10}/\sqrt{2}$ and $iHG_{01}/\sqrt{2}$, providing position information about both x and y. *(D)* Scattering patterns for the modes, illustrating how information is encoded in the angular distribution.

5.4.3 Projecting information forward

The use of the fundamental Gaussian beam results in an information pattern where most of the information is directed backward, as illustrated in (Fig. 5.4A). In contrast, employing a Hermite-Gaussian $HG_{m=2,n=0}$ mode produces an information pattern that directs most of the information forward. This behavior arises from the steeper Gouy phase shift near the origin associated with higher-order modes. Such a forward-scattering configuration could significantly reduce the overhead of implementing phase stabilization in interferometric setups, as the forward-scattered light remains collinear with the original incident field, simplifying phase reference alignment compared to backscattered light.

To fully understand this phenomenon, a non-paraxial analysis of the Gouy phase anomaly should be conducted, as deviations from paraxial approximations may influence the scattering patterns and their practical implications in interferometry.

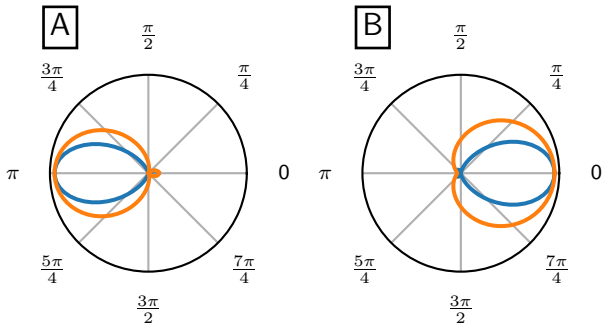

Figure 5.4: **A:** Angular distribution of information for Gaussian beam. **B:** Angular distribution of information for Hermite-Gauss $m = 2, n = 0$ beam. The pattern is not axially simetric along z but has a broader xz profile

5.4.4 Decoherence on rotating saddle beam

Stable optical trapping has been proposed in a structured beam with an intensity profile resembling a saddle [80]. The saddle trap involves a situation where the light field and its gradient vanish in the center of the trap and (Eq. 5-38) do not convey information about the particle's position to first order in the dipole interaction. Furthermore, second-order effects, being even functions, cannot provide which-path information for superposition states involving diametrically opposed coherence on position basis [81, 82]. Specifically, the localization term for such states vanishes, $\rho_{\text{loc}}(x, -x) = -\frac{\Gamma}{2}\langle x|[x^2, [x^2, \rho]]| - x\rangle = 0$. This symmetry ensures that decoherence is suppressed, and can become a useful resource for experiments aiming to produce quantum superposition states.

Parametric cooling requires actuating on the laser power at the second harmonic of the position signal. In systems with linear position readout, such as Gaussian beam trap, the direct signal must be processed externally with electronics to generate the second harmonic. Once extracted, this second harmonic provides a pathway to cool the particle's mechanical state using a parametric modulation. This approach leverages the harmonic response to effectively dissipate energy from the mechanical degrees of freedom.

The information provided by the saddle trap is encoded in the second harmonic of the particle's signal. This direct redout can be effectively utilized to cool the particle's mechanical state through parametric modulation [81]. Such an approach offers a promising pathway toward quantum states, enabling the preparation of cold mechanical states while preserving the quantum coherences that are crucial for advancing quantum applications.

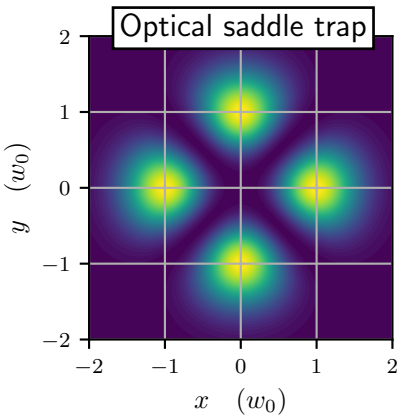

Figure 5.5: **A:** Light field configuration that does not provide information on linear order in the dipole interaction.

6
Outlook

Optical levitation provides a robust platform for stably trapping nanoparticles, intrinsically integrating position readout and enabling precise control over their mechanical motion. The center-of-mass motion of a nanoparticle has already been cooled to its quantum ground state [24, 25, 26, 27, 28]. However, the preparation of nonclassical motional states remains a formidable challenge, predominantly due to intrinsic recoil heating and decoherence mechanisms originating from the same light field employed for trapping and control.

A significant limitation arises from the mismatch between the spatial scale of readily available nonlinearities and the coherence length of quantum states. The intrinsic nonlinearity of the optical potential is fundamentally constrained by the diffraction limit of the beam, typically on the order of 500 nm, while the spatial extent of the ground-state wavefunction is only a few picometers. Expanding the ground-state wavefunction while preserving the particle's mechanical energy is an inherently challenging task. Furthermore, maintaining quantum coherence is particularly demanding: photons interacting with the particle continuously encode positional information, even in the absence of significant momentum transfer, rendering the high photon flux a highly effective source of decoherence.

Recent experiments have shown initial progress toward achieving coherent expansion of quantum states. However, the gap between current capabilities and the requirements for the robust generation of quantum non-Gaussian states remains substantial, with improvements still needed across several orders of magnitude to enable truly impactful implementations.

Based on the findings presented in this thesis, we propose two potential approaches to address this issue. The first approach involves coupling external, sharper nonlinearities to the system, effectively reducing the spatial extent over which they dominate. This enables the preparation of smaller states, which helps mitigate decoherence effects by minimizing the spatial footprint of the system. The second approach seeks to induce nonlinearities through the use of tailored light fields engineered to greatly suppress position localization decoherence.

Coupling nonlinearities can be achieved by electronically processing position signals and feeding them back into the system, as demonstrated in the proof-of-principle experiment described in Chapter 3. This approach provides a promising pathway for the controlled generation of non-Gaussian states with

reduced spatial extent. These states are expected to exhibit greater resilience to recoil heating and decoherence, particularly when their spatial spread is maintained significantly smaller than the photon wavelength, where positional resolution becomes inherently limited.

Further refinement of these methods could enable the preparation of non-Gaussian states with reduced occupation numbers, which is expected to promote the emergence of quantum coherence. In addition to utilizing external electric forces with non-homogeneous characteristics, parametric modulation of the optical trap—carefully designed to induce nonlinearity and damping—offers a promising pathway for accessing and stabilizing low-occupation-number non-Gaussian states. Preliminary computer simulations have demonstrated the feasibility of this approach, indicating that experimental implementation is within reach. This method provides a significant advantage by maintaining the particle trapped throughout the state preparation process, thereby avoiding the complexities associated with free-flight protocols.

However, it is important to note that electronic noise introduced during signal processing could create a new decoherence channel, potentially offsetting the benefits of this approach. Mitigating such noise will be essential to ensure the robustness of the method and preserve the coherence of the prepared states. It is also likely that partial progress will initially be made by generating statistical mixtures of high-quality bimodal states before achieving the preparation of true quantum non-Gaussian states. Such intermediate results could provide valuable insights and benchmarks for advancing toward fully quantum non-Gaussian state generation.

In the second approach, optical fields are employed to suppress decoherence. Structured optical gratings, constructed from tailored light fields, offer a promising method for generating non-Gaussian parity-position states. For this approach to be effective, these gratings must be meticulously designed to minimize decoherence while maximizing the interaction time between the particle and the structured optical field. However, these optical fields are not inherently confining and instead act as gratings through which the particle must traverse. Protocols such as 'throw-and-catch,' where the particle is temporarily released and later recaptured, present a potential strategy for extending interaction times. Nevertheless, recapturing the particle in shallow traps introduces significant engineering challenges, particularly due to the combined effects of gravitational free flight and the limited depth of optical traps.

Practical implementation of this approach remains an open challenge. Spatial light modulators (SLMs) are inherently inefficient, with significant reductions in output power. Additionally, the efficiency of SLMs varies de-

pending on the programmed field output, introducing further limitations that compromise consistent performance. Moreover, the response time of SLMs is significantly slower than the timescales of particle dynamics and the protocol requirements, making them unsuitable for real-time adjustments. Addressing these issues will be crucial for the successful realization of this method.

7
Bibliography

[1] KEPLER, J. De cometis libelli tres. i. astronomicvs,... ii. physicvs,... iii. astrologicvs,... *(No Title)*. Cited in page 18.

[2] POYNTING, J. H. On the transfer of energy in the electromagnetic field. *Proceedings of the Royal Society of London*, The Royal Society London, v. 36, n. 228-231, p. 186–187, 1883. Cited in page 18.

[3] NICHOLS, E. F.; HULL, G. F. A preliminary communication on the pressure of heat and light radiation. *Physical Review (Series I)*, APS, v. 13, n. 5, p. 307, 1901. Cited in page 18.

[4] LEBEDEW, P. Untersuchungen über die druckkräfte des lichtes. *Annalen der Physik*, Wiley Online Library, v. 311, n. 11, p. 433–458, 1901. Cited in page 18.

[5] EINSTEIN, A. On the development of our views concerning the nature and constitution of radiation. *Phys. Z*, v. 10, n. 22, p. 817–825, 1909. Cited in page 18.

[6] BRAGINSKI, V.; MANUKIN, A. Ponderomotive effects of electromagnetic radiation. *Sov. Phys. JETP*, v. 25, n. 4, p. 653–655, 1967. Cited in page 18.

[7] BRAGINSKIĭ, V.; MANUKIN, A. B.; TIKHONOV, M. Y. Investigation of dissipative ponderomotive effects of electromagnetic radiation. *Soviet Journal of Experimental and Theoretical Physics*, v. 31, p. 829, 1970. Cited in page 18.

[8] ASHKIN, A. et al. Observation of a single-beam gradient force optical trap for dielectric particles. *Optics Letters*, Optica Publishing Group, v. 11, n. 5, p. 288–290, 1986. Cited in page 18.

[9] CAVES, C. M. Quantum-mechanical radiation-pressure fluctuations in an interferometer. *Physical Review Letters*, APS, v. 45, n. 2, p. 75, 1980. Cited in page 18.

[10] ASPELMEYER, M.; KIPPENBERG, T. J.; MARQUARDT, F. Cavity optomechanics. *Reviews of Modern Physics*, APS, v. 86, n. 4, p. 1391–1452, 2014. Cited in page 18.

[11] BOWEN, W. P.; MILBURN, G. J. *Quantum optomechanics*. [S.l.]: CRC press, 2015. Cited in page 18.

[12] JONES, P. H.; MARAGÒ, O. M.; VOLPE, G. *Optical tweezers: Principles and applications*. [S.l.]: Cambridge University Press, 2015. Cited in page 18.

[13] GIESELER, J. et al. Optical tweezers—from calibration to applications: a tutorial. *Advances in Optics and Photonics*, Optica Publishing Group, v. 13, n. 1, p. 74–241, 2021. Cited 2 times in pages 18 and 31.

[14] ROMERO-ISART, O. et al. Large quantum superpositions and interference of massive nanometer-sized objects. *Physical review letters*, APS, v. 107, n. 2, p. 020405, 2011. Cited in page 18.

[15] DANIA, L. et al. Ultrahigh quality factor of a levitated nanomechanical oscillator. *Physical Review Letters*, APS, v. 132, n. 13, p. 133602, 2024. Cited 2 times in pages 19 and 66.

[16] GONZALEZ-BALLESTERO, C. et al. Levitodynamics: Levitation and control of microscopic objects in vacuum. *Science*, American Association for the Advancement of Science, v. 374, n. 6564, p. eabg3027, 2021. Cited in page 19.

[17] ARNDT, M.; HORNBERGER, K. Testing the limits of quantum mechanical superpositions. *Nature Physics*, Nature Publishing Group UK London, v. 10, n. 4, p. 271–277, 2014. Cited in page 19.

[18] CARNEY, D.; STAMP, P. C.; TAYLOR, J. M. Tabletop experiments for quantum gravity: a user's manual. *Classical and Quantum Gravity*, IOP Publishing, v. 36, n. 3, p. 034001, 2019. Cited in page 19.

[19] YOUNG, T. Ii. the bakerian lecture. on the theory of light and colours. *Philosophical transactions of the Royal Society of London*, The Royal Society London, n. 92, p. 12–48, 1802. Cited in page 20.

[20] THOMSON, G. P.; REID, A. Diffraction of cathode rays by a thin film. *Nature*, Nature Publishing Group UK London, v. 119, n. 3007, p. 890–890, 1927. Cited in page 20.

[21] ARNDT, M. et al. Wave–particle duality of c60 molecules. *nature*, Nature Publishing Group UK London, v. 401, n. 6754, p. 680–682, 1999. Cited in page 20.

[22] EIBENBERGER, S. et al. Matter–wave interference of particles selected from a molecular library with masses exceeding 10000 amu. *Physical Chemistry Chemical Physics*, Royal Society of Chemistry, v. 15, n. 35, p. 14696–14700, 2013. Cited in page 20.

[23] FEIN, Y. Y. et al. Quantum superposition of molecules beyond 25 kda. *Nature Physics*, Nature Publishing Group UK London, v. 15, n. 12, p. 1242–1245, 2019. Cited in page 20.

[24] DELIĆ, U. et al. Cooling of a levitated nanoparticle to the motional quantum ground state. *Science*, American Association for the Advancement of Science, v. 367, n. 6480, p. 892–895, 2020. Cited 3 times in pages 20, 58, and 80.

[25] TEBBENJOHANNS, F. et al. Quantum control of a nanoparticle optically levitated in cryogenic free space. *Nature*, Nature Publishing Group UK London, v. 595, n. 7867, p. 378–382, 2021. Cited 5 times in pages 20, 41, 44, 58, and 80.

[26] MAGRINI, L. et al. Real-time optimal quantum control of mechanical motion at room temperature. *Nature*, Nature Publishing Group UK London, v. 595, n. 7867, p. 373–377, 2021. Cited 4 times in pages 20, 44, 58, and 80.

[27] KAMBA, M.; SHIMIZU, R.; AIKAWA, K. Optical cold damping of neutral nanoparticles near the ground state in an optical lattice. *Optics Express*, Optica Publishing Group, v. 30, n. 15, p. 26716–26727, 2022. Cited 3 times in pages 20, 58, and 80.

[28] PIOTROWSKI, J. et al. Simultaneous ground-state cooling of two mechanical modes of a levitated nanoparticle. *Nature Physics*, Nature Publishing Group UK London, v. 19, n. 7, p. 1009–1013, 2023. Cited 2 times in pages 20 and 80.

[29] BATEMAN, J. et al. Near-field interferometry of a free-falling nanoparticle from a point-like source. *Nature communications*, Nature Publishing Group UK London, v. 5, n. 1, p. 4788, 2014. Cited in page 20.

[30] RODA-LLORDES, M. et al. Macroscopic quantum superpositions via dynamics in a wide double-well potential. *Physical Review Letters*, APS, v. 132, n. 2, p. 023601, 2024. Cited in page 20.

[31] NEUMEIER, L. et al. Fast quantum interference of a nanoparticle via optical potential control. *Proceedings of the National Academy of Sciences*, National Acad Sciences, v. 121, n. 4, p. e2306953121, 2024. Cited in page 20.

[32] WARDAK, J. et al. Nanoparticle interferometer by throw and catch. *Atoms*, MDPI, v. 12, n. 2, p. 7, 2024. Cited in page 20.

[33] ROSSI, M. et al. Quantum delocalization of a levitated nanoparticle. *arXiv preprint arXiv:2408.01264*, 2024. Cited in page 20.

[34] WU, Q. et al. Squeezing below the ground state of motion of a continuously monitored levitating nanoparticle. *Quantum Science and Technology*, 2024. Cited in page 20.

[35] WALSCHAERS, M. Non-gaussian quantum states and where to find them. *PRX quantum*, APS, v. 2, n. 3, p. 030204, 2021. Cited in page 21.

[36] RODA-LLORDES, M. et al. Macroscopic quantum superpositions via dynamics in a wide double-well potential. *arXiv preprint arXiv:2303.07959*, 2023. Cited in page 21.

[37] RAKHUBOVSKY, A. A.; MOORE, D. W.; FILIP, R. Nonclassical states of levitated macroscopic objects beyond the ground state. *Quantum Science and Technology*, IOP Publishing, v. 4, n. 2, p. 024006, 2019. Cited in page 21.

[38] VANNER, M. et al. Cooling-by-measurement and mechanical state tomography via pulsed optomechanics. *Nature communications*, Nature Publishing Group UK London, v. 4, n. 1, p. 2295, 2013. Cited in page 21.

[39] RASHID, M.; TOROŠ, M.; ULBRICHT, H. Wigner function reconstruction in levitated optomechanics. *Quantum Measurements and Quantum Metrology*, De Gruyter Open, v. 4, n. 1, p. 17–25, 2017. Cited 2 times in pages 21 and 61.

[40] VANNER, M. R.; PIKOVSKI, I.; KIM, M. Towards optomechanical quantum state reconstruction of mechanical motion. *Annalen der Physik*, Wiley Online Library, v. 527, n. 1-2, p. 15–26, 2015. Cited in page 21.

[41] SHAHANDEH, F.; RINGBAUER, M. Optomechanical state reconstruction and nonclassicality verification beyond the resolved-sideband regime. *Quantum*, Verein zur Förderung des Open Access Publizierens in den Quantenwissenschaften, v. 3, p. 125, 2019. Cited in page 21.

[42] WARSZAWSKI, P. et al. Tomography of an optomechanical oscillator via parametrically amplified position measurement. *New Journal of Physics*, IOP Publishing, v. 21, n. 2, p. 023020, 2019. Cited in page 21.

[43] WEISS, T.; ROMERO-ISART, O. Quantum motional state tomography with nonquadratic potentials and neural networks. *Physical Review Research*, APS, v. 1, n. 3, p. 033157, 2019. Cited in page 21.

[44] HARADA, Y.; ASAKURA, T. Radiation forces on a dielectric sphere in the rayleigh scattering regime. *Optics communications*, Elsevier, v. 124, n. 5-6, p. 529–541, 1996. Cited in page 24.

[45] ASHKIN, A. Acceleration and trapping of particles by radiation pressure. *Physical review letters*, APS, v. 24, n. 4, p. 156, 1970. Cited in page 24.

[46] OMORI, R.; KOBAYASHI, T.; SUZUKI, A. Observation of a single-beam gradient-force optical trap for dielectric particles in air. *Optics letters*, Optica Publishing Group, v. 22, n. 11, p. 816–818, 1997. Cited in page 24.

[47] JAIN, V. et al. Direct measurement of photon recoil from a levitated nanoparticle. *Physical review letters*, APS, v. 116, n. 24, p. 243601, 2016. Cited in page 28.

[48] GIESELER, J.; NOVOTNY, L.; QUIDANT, R. Thermal nonlinearities in a nanomechanical oscillator. *Nature Physics*, Nature Publishing Group UK London, v. 9, n. 12, p. 806–810, 2013. Cited 4 times in pages 28, 37, 43, and 57.

[49] KUBO, R. The fluctuation-dissipation theorem. *Reports on Progress in Physics*, IOP Publishing, v. 29, n. 1, p. 255, 1966. Cited in page 31.

[50] HEBESTREIT, E. et al. Calibration and energy measurement of optically levitated nanoparticle sensors. *Review of Scientific Instruments*, AIP Publishing, v. 89, n. 3, 2018. Cited 2 times in pages 31 and 49.

[51] SUASSUNA, B.; MELO, B.; GUERREIRO, T. Path integrals and nonlinear optical tweezers. *Phys. Rev. A*, American Physical Society, v. 103, p. 013110, Jan 2021. Disponível em: <https://link.aps.org/doi/10.1103/PhysRevA.103.013110>. Cited 8 times in pages 33, 34, 35, 36, 43, 44, 47, and 48.

[52] KREMER, O. et al. Perturbative nonlinear feedback forces for optical levitation experiments. *Physical Review A*, APS, v. 109, n. 2, p. 023521, 2024. Cited in page 33.

[53] CHOW, C. C.; BUICE, M. A. Path integral methods for stochastic differential equations. *The Journal of Mathematical Neuroscience (JMN)*, Springer, v. 5, p. 1–35, 2015. Cited 2 times in pages 34 and 36.

[54] CUAIRAN, M. T. et al. Precision calibration of the duffing oscillator with phase control. *Physical Review Letters*, APS, v. 128, n. 21, p. 213601, 2022. Cited in page 34.

[55] INNERBICHLER, M. et al. White-noise fluctuation theorem for langevin dynamics. *New Journal of Physics*, IOP Publishing, v. 24, n. 11, p. 113028, 2022. Cited in page 37.

[56] TEBBENJOHANNS, F. et al. Cold damping of an optically levitated nanoparticle to microkelvin temperatures. *Physical review letters*, APS, v. 122, n. 22, p. 223601, 2019. Cited in page 41.

[57] CONANGLA, G. P. et al. Optimal feedback cooling of a charged levitated nanoparticle with adaptive control. *Physical review letters*, APS, v. 122, n. 22, p. 223602, 2019. Cited in page 41.

[58] BULLIER, N.; PONTIN, A.; BARKER, P. Quadratic optomechanical cooling of a cavity-levitated nanosphere. *Physical Review Research*, APS, v. 3, n. 3, p. L032022, 2021. Cited in page 44.

[59] LLOYD, S.; SLOTINE, J.-J. E. Quantum feedback with weak measurements. *Physical Review A*, APS, v. 62, n. 1, p. 012307, 2000. Cited in page 44.

[60] SCHAUMANN, R.; XIAO, H.; MAC, V. V. *Design of analog filters*. 2nd. ed. [S.l.]: Oxford University Press, Inc., 2009. Cited in page 47.

[61] WILSON, P. *Design recipes for FPGAs*. [S.l.]: Newnes, 2015. Cited in page 48.

[62] RICCI, F. et al. Accurate mass measurement of a levitated nanomechanical resonator for precision force-sensing. *Nano letters*, ACS Publications, v. 19, n. 10, p. 6711–6715, 2019. Cited in page 49.

[63] MUFFATO, R. et al. Generation of classical non-gaussian distributions by squeezing a thermal state into non-linear motion of levitated optomechanics. *arXiv preprint arXiv:2401.04066*, 2024. Cited in page 50.

[64] RASHID, M. et al. Experimental realization of a thermal squeezed state of levitated optomechanics. *Physical Review Letters*, APS, v. 117, n. 27, p. 273601, 2016. Cited in page 50.

[65] SETTER, A.; VOVROSH, J.; ULBRICHT, H. Characterization of nonlinearities through mechanical squeezing in levitated optomechanics. *Applied Physics Letters*, AIP Publishing, v. 115, n. 15, 2019. Cited in page 51.

[66] FRIMMER, M. et al. Rapid flipping of parametric phase states. *Physical review letters*, APS, v. 123, n. 25, p. 254102, 2019. Cited in page 51.

[67] RICCI, F. et al. Optically levitated nanoparticle as a model system for stochastic bistable dynamics. *Nature communications*, Nature Publishing Group UK London, v. 8, n. 1, p. 15141, 2017. Cited in page 51.

[68] GIESELER, J. et al. Dynamic relaxation of a levitated nanoparticle from a non-equilibrium steady state. *Nature nanotechnology*, Nature Publishing Group UK London, v. 9, n. 5, p. 358–364, 2014. Cited in page 51.

[69] GIESELER, J. et al. Nonlinear mode coupling and synchronization of a vacuum-trapped nanoparticle. *Physical review letters*, APS, v. 112, n. 10, p. 103603, 2014. Cited in page 51.

[70] MILITARU, A. et al. Escape dynamics of active particles in multistable potentials. *Nature Communications*, Nature Publishing Group UK London, v. 12, n. 1, p. 2446, 2021. Cited in page 51.

[71] COSCO, F.; PEDERNALES, J.; PLENIO, M. B. Enhanced force sensitivity and entanglement in periodically driven optomechanics. *Physical Review A*, APS, v. 103, n. 6, p. L061501, 2021. Cited in page 51.

[72] VOVROSH, J. et al. Parametric feedback cooling of levitated optomechanics in a parabolic mirror trap. *JOSA B*, Optica Publishing Group, v. 34, n. 7, p. 1421–1428, 2017. Cited 3 times in pages 52, 53, and 58.

[73] ASHMAN, K. M.; BIRD, C. M.; ZEPF, S. E. Detecting bimodality in astronomical datasets. *Astron. J.*, v. 108, p. 2348, 1994. Cited in page 57.

[74] KIRCHMAIR, G. et al. Observation of quantum state collapse and revival due to the single-photon kerr effect. *Nature*, Nature Publishing Group UK London, v. 495, n. 7440, p. 205–209, 2013. Cited in page 58.

[75] ROSIEK, C. A. et al. Quadrature squeezing enhances wigner negativity in a mechanical duffing oscillator. *PRX Quantum*, APS, v. 5, n. 3, p. 030312, 2024. Cited in page 58.

[76] RANFAGNI, A. et al. Two-dimensional quantum motion of a levitated nanosphere. *Physical Review Research*, APS, v. 4, n. 3, p. 033051, 2022. Cited in page 58.

[77] KREMER, O. et al. All-electrical cooling of an optically levitated nanoparticle. *Physical Review Applied*, APS, v. 22, n. 2, p. 024010, 2024. Cited in page 58.

[78] FEYNMAN, R. P.; HIBBS, A. R.; STYER, D. F. *Quantum mechanics and path integrals*. [S.l.]: Courier Corporation, 2010. Cited in page 61.

[79] TEBBENJOHANNS, F.; FRIMMER, M.; NOVOTNY, L. Optimal position detection of a dipolar scatterer in a focused field. *Physical Review A*, APS, v. 100, n. 4, p. 043821, 2019. Cited in page 74.

[80] TANDEITNIK, D. et al. All-optical saddle trap. *Physical Review Applied*, APS, v. 22, n. 4, p. 044073, 2024. Cited in page 78.

[81] GAJEWSKI, R.; BATEMAN, J. Backaction suppression in levitated optomechanics using reflective boundaries. *arXiv preprint arXiv:2405.04366*, 2024. Cited in page 78.

[82] WEISER, Y. et al. Back action suppression for levitated dipolar scatterers. *arXiv preprint arXiv:2402.04802*, 2024. Cited in page 78.